ANNEX

IMPLEMENTING STEREOTACTIC RAPIDARC TREATMENTS INTO CLINICAL ROUTINE:
FROM ALGORITHM CONFIGURATION TO TREATMENT VALIDATION

A. Van Esch [1,2,3], F. Sergent [2,3], K. Basta [3], P. Bertrand[4], C. Corbice[4], E. Fontaine[4], L. Hambach[2], A. Blavier[2], C. Clermont[2], D.P. Huyskens[1,2,3]

[1] 7Sigma, QA-team in radiotherapy physics, Kasteeldreef 2, 3150 Tildonk, Belgium

[2] Université catholique de Louvain, CHU-UCL Namur, Service de radiothérapie, Place L Godin 15, 5000 Namur, Belgium

[3] Centre Hospitalier de Mouscron, Avenue de Fécamp 49, 7700 Mouscron, Belgium

[4] CHU de la Réunion, Site GHSR, Av. Francois Mitterand BP305, 97448 Saint-Pierre, Réunion

Abstract: **Purpose: This work aims to aid the medical physicist with the safe implementation of RapidArc (RA) (Varian Medical Systems, Palo Alto, CA) stereotactic radiotherapy treatments (SRS/SBRT) into clinical routine, from treatment planning system (TPS) configuration to patient plan verification. Implementation procedures are applicable to different Varian linear accelerators, either equipped with a standard Millennium 120MLC or a high-definition HDMLC, but always with on-board imaging.**

Methods: A systematic approach was used to assure proper control of the different aspects of the implementation. First, an extensive series of detectors (all from PTW, Freiburg, Germany) – from numerous single detectors to the 1000SRS/Octavius4D 3D dose measurement system - were carefully benchmarked to assess their dosimetric characteristics, their precision and their practical usefulness. This benchmarking was performed independently of the TPS. Second, the necessary measurements were performed to include small field data in the Analytical Anisotropic Algorithm (AAA) and Acuros (AXB) algorithm configuration. Third, validation of the Eclipse small field dose calculation was performed for both algorithms, starting off with static gantry (small) MLC fields and ending with RA SRS/SBRT test plans. Finally, pre-treatment QA procedures were implemented, executed and analyzed on all patient treatments.

Results: While one can do a substantial part of the basic validation with a single, high resolution, directionally independent detector, a water phantom and a small solid water phantom to hold this detector, a single measurement is insufficient to assess the geometric precision of the dose-fall off during arc delivery. Given the safety requirements for stereotactic treatments, it is therefore highly recommended to invest in a detector system that can provide 2D and 3D dose information as well. The 1000SRS was found to provide very reliable planar dose measurements and, in combination with the Octavius4D system, measurement-based 3D dose reconstructions. It is also the most efficient method, especially when multiple lesions are concerned. From the battery of validation measurements, it was found that, although the algorithm configuration as well as the MLC modeling within the Eclipse TPS could benefit from further improvements, the currently obtained results are within clinical acceptance for the specific requirements of stereotactic treatment plans.

Conclusions: Target localization remains the key aspect of successful stereotactic radiotherapy and should be carefully addressed according to the treatment site. However, from a dosimetric point of view, when the appropriate measurement equipment is available, safe implementation of stereotactic RA treatments should be within reach of all radiotherapy departments outfitted with an up to date Clinac (or TrueBeam) and state-of-the-art on-board imaging.

I. INTRODUCTION

Intracranial brain lesions have long been treated with stereotactic radiosurgery (SRS) on equipment specifically dedicated to this high dose, high precision technique. Gradually, the extremely hypofractionated treatment technique has expanded to include small lesions outside of the brain and spine, introducing stereotactic body radiotherapy (SBRT) in e.g. liver and lung. Delivering such high doses per fraction requires high conformity and steep dose fall-off to avoid irradiating organs at risk. It necessitates appropriate patient immobilisation and image-guidance for patient set-up. Technology has evolved significantly since the onset of SRS/SBRT. Current day linear accelerators have gained in geometric and dosimetric precision, allow more advanced treatment optimisation and delivery techniques such as IMRT and VMAT, and are often standard equipped with on-board kV imaging and CBCT. Because of the rising amount of literature reporting favourable therapeutic outcome of SRS/SBRT for a variety of clinical indications [1-12], it is no wonder that there is a growing interest to implement SRS/SBRT treatments on these widely available treatment units. Although requirements for immobilization, treatment planning and delivery can vary significantly with disease site, quality assurance and safety issues are similar: the delivery of high dose fractions implies that the margin of error is much smaller than for conventional radiotherapy. Even small inaccuracies in target localization can lead to serious under-treatment of the target or severe overdosage to the adjacent normal tissue. When adjacent normal tissue includes high-risk organs, fractionated stereotactic radiotherapy (FSRT)

can be used to provide additional normal tissue protection [13].

While the most essential aspect of all stereotactic treatments is undoubtedly the high precision treatment localization during all steps of the treatment process, implementing this treatment technique into clinical routine also presents challenges from a dosimetric point of view as small field dosimetry comes with its own specific problems [14]. Reports of past accidents are an unfortunate testimony of this [15-20]. Given the beneficial therapeutic possibilities when stereotactic treatments are made available, it is therefore the purpose of this work to provide practical guidelines on the safe implementation of stereotactic treatments on readily available radiotherapy equipment, more specifically, on Varian (Varian Medical Systems, Palo Alto, CA) linear accelerators in combination with the Varian Eclipse treatment planning system (TPS). As stereotactic treatments on the Novalis (Brainlab, Feldkirchen, Germany) linear accelerator in combination with the dedicated iPlan TPS (Brainlab) have been around for a while, this is a well-established solution and numerous publications on the subject already exist [21-25]. The iPlan stereotactic treatments are primarily non-coplanar, conformal arc treatments. The standard dose calculation algorithm in the iPlan software is the single pencil beam model. It is robust and works well for SRS. It is unfortunately less well adapted for SBRT, especially in highly heterogeneous media such as lung. With the availability of VMAT (RapidArc® (RA)) in combination with the more advanced dose calculation algorithms such as the Anisotropic Analytical Algorithm (AAA) and Acuros (AXB) in the Eclipse planning system, there is a growing desire to include stereotactic treatment planning into the Varian integrated environment. A number of publications exist on this subject already [26-41], presenting mostly planning studies but also reporting clinical treatments. On the topic of dose calculations in lung lesions, planning studies present a comparison between the AAA and AXB calculations or compare the respective dose calculations to measurements in heterogeneous phantoms. Conclusions are unanimous: AXB dose calculations are superior to AAA when it comes to heterogeneity corrections. While lung SBRT is very sensitive to the heterogeneity correction method, it is less dependent on small field dosimetry as the lung lesions generally require larger field sizes than cranial SRS. It is even so that for lung SBRT, the Eclipse dose calculation algorithms often do not even have to be specially configured below the standard minimum field size of $3x3cm^2$. This does not hold for cranial SRS for which the small field data definitely need to be added to the algorithm configuration. Initial assessments of the AAA and AXB accuracy for small fields were reported and found to be promising [42]. Numerous and elaborate guidelines on TPS validation for stereotactic treatments exist, but these are all general guiding principles and not solution specific [14]. In addition, with the rising interest in stereotactic treatments, improved single detectors and user friendly 2D and 3D measurement devices have

become commercially available relatively recently, potentially liberating the medical physicist from the tedious and error prone film or gel dosimetry. Dosimetric characteristics of almost all of the available detectors have been reported in literature, but mostly on a fundamental basis and not in the framework of TPS-specific usefulness [43, 44-46]. Silicon diode detectors are commonly used but are not dosimetrically water equivalent, resulting in energy dependence and fluence perturbation for field sizes with a dimension below 1 cm. The relatively new synthetic microDiamond (PTW, Freiburg, Germany) detector provides superior water equivalence to diode detectors but has a slightly larger cross-section than diodes. It has become clear that, up to date, there is no real-time detector available that can accurately measure output factors down to field sizes of 5 mm without the use of correction factors. Numerous groups have worked to derive appropriate correction factors through comparison with Monte Carlo simulations, Gafchromic EBT2 film and plastic scintillators [47, 48, 49]. Unfortunately, beyond field dimensions of the order of 1 cm, the exact values of the tabulated correction factors differ between publications, sometimes by considerable amounts. The origin of the differences is difficult to trace, but they at offer another illustration of the delicacy of small field data acquisition. It is, however, not the goal of our work to elaborate on the small(est) field correction factors. On the contrary, while these factors may be applicable for stereotactic dose delivery through cones or other fixed field apertures, their practical use in modulated stereotactic treatment delivery is unfortunately very limited. Even for the simple output factor measurements, while correction factors exist for a 1x1 cm² field, rectangular fields up to 1x40 cm² need to be acquired for algorithm configuration and there are no published values for these narrow, elongated field dimensions. Moreover, in clinical practice, when validating patient treatments consisting of modulated fields with aperture openings that vary during delivery, applying such correction factors is simply not feasible from a practical point of view. In this study, we therefore study the different detectors without the use of any field size dependent correction factor. This more pragmatic approach allows us to assess which detectors qualify for use in clinical practice when varying beam apertures complicate the use of appropriate correction factors.

The extensive literature on different detectors can be overwhelming and does not necessarily facilitate the choice. It is, however, important to not blindly select a detector based on its fundamental properties but to also take into account the practical implications of the detector choice for the task at hand. As the latter are often hard to judge without actually purchasing the equipment, we have tried to present a practical overview specific to the needs of the Eclipse TPS and the RapidArc treatment modality.

The manuscript outlines a procedure for performing basic benchmarking of available QA equipment. Once the behaviour of the chosen detector(s) has been confirmed and/or quantified, one can proceed to the small-field specific

algorithm (AAA or AXB) configuration and subsequent validation. As a final step, possible patient QA procedures are addressed and compared. With the QA steps outlined from start to finish, we hope to aid the medical physicist with the safe implementation of stereotactic RA treatments into clinical routine.

As VMAT optimization offers new possibilities for optimizing the dose distribution to the target, the traditional non-uniform stereotactic target coverage can now be made more homogeneous through VMAT delivery. Whether or not the customary 70 to 100% dose gradient in the target needs to be maintained or whether it would be beneficial to strive towards a more uniform dose distribution, is a clinical debate and beyond the scope of this work. On a similar note, now that the treatment beam output within an arc can be better optimized, the need for elaborate couch rotations should be subjected to critical revision. Reducing the number of couch rotations in a plan facilitates accurate patient localization by means of the on-board imaging and therefore merits serious consideration. Although the actual RA optimization is again not the subject of this manuscript, the choice of treatment geometry does have an impact on the possible QA procedures. We therefore address all geometries, from drastically non-coplanar to entirely coplanar arc delivery.

For the medical physicist, dosimetric issues are similar between SRS, SBRT and FSRT as they are mostly related to the small field size rather than to the dose per fraction. For the purpose of this work, we will therefore reduce the amount of acronyms used and refer to all of the above as stereotactic radiotherapy (SRT).

II. METHODS AND MATERIALS

All data were acquired on either a Clinac iX (Varian) dual energy accelerator (6&18 MV (at CH Mouscron), 6&23 MV(at CHU Réunion)) equipped with a 120 Millennium MLC (120MLC) or on a NovalisTX (Brainlab) (at CHU Namur) linear accelerator (6MV, 6MV_SRS and 18MV) equipped with the high definition MLC (HDMLC). The focus being on stereotactic treatments, all presented data in this work concern the 6MV or 6MV_SRS treatment beams. The Clinac iX units have a Varian IGRT treatment couch while the NovalisTX treatment unit has a Brainlab Exact couch. Both can perform on-board imaging (kV, MV (aS1000) and CBCT) while the NovalisTX has an additional ExacTrac (Brainlab) positioning system. Stereotactic treatments in routine can either be planned as RapidArc treatments with the Eclipse treatment planning system (Varian), or as conformal arc treatments with either Eclipse or the iPlan software (Brainlab). While conformal arcs were used in the validation process, the final objective is to use RA delivery for SRT patient treatments. In Eclipse, dose distributions were calculated by means of the Analytical Anisotropic Algorithm (AAA v11.0.31) or the Acuros (AXB v11.0.31) algorithm.

Table 1: Overview of PTW detector characteristics relevant to stereotactic data acquisition. the electron diode dE (TW60012), the stereotactic diode dSRS (TW60018), the photon diode dP (TW60008), the microDiamond μD (TN60019), the 3D PinPoint Pp3D (TN31016) and the Semiflex3D Sf3D (TN31021). Although the Octavius1500 and 1000SRS (both PTW, Freiburg, Germany) are two-dimensional arrays rather than single detectors, their presence in table 1 serves to characterise the individual ion chambers of the 2D composition.

	dE	dSRS	dP	μD	Pp3D$_{rad}$	Pp3D$_{ax}$	Sf3D	1000SRS	Oct1500
radius (cm) (vendor given)	0.06	0.06	0.06	0.11	0.145+	0.145	0.275++	~0.16+++	~0.28++++
sensitivity (nC/Gy) (measured)	169.8	169.4	130.0	1.1	0.4	0.4	2.0	/	/
Field size dependence (normalised to 5x5 cm^2 open field dose and relative to μD measurement)									
MLC in XxY (cm^2)									
0.5x0.5 in 1x1	1.025	1.032	1.025	1.000	0.773	0.839	0.492	1.038	0.606
0.5x1 in 1x2	1.012	1.022	1.012	1.000	0.888	0.931	0.693	1.029	0.892
1x1 in 2x2	1.005	1.009	0.999	1.000	0.929	0.962	0.818	1.021	0.971
2x2 in 3x3	1.000	1.000	0.999	1.000	0.992	0.996	0.988	1.010	0.966
3x3 in 5x5	1.000	1.000	0.999	1.000	1.002	0.999	1.000	1.004	0.989
5x5 (no MLC)	1.000	1.000	1.000	1.000	1.000	1.000	1.000	1.000	1.000
Directional dependence (relative to axial measurement in Ruby)									
Gantry rotation (couch 90°)									
315	0.93	0.92	0.71	1.00	1.01	/	1.00	/	/
0	0.90	0.89	0.83	1.00	1.00	/	1.00	/	/
45	0.97	0.966	0.98	1.01	1.00	/	1.00	/	/
90	1.00	1.00	1.00	1.00	1.00	/	1.00	/	/

+ length = 2.9 mm, ++ length = 6.5 mm, +++ volume = 2.3x2.3x0.5 mm^3, ++++ volume = 4.4x4.4x3 mm^3

At the onset of the implementation of SRT treatments, it is most essential to first quantify the mechanical precision of the different components. By means of the Winston-Lutz test [53] (or an in-house developed equivalent setup) and the portal imager, we have quantified the mechanical precision of the isocentric rotation of the gantry, the collimator, the treatment couch and the on-board imaging. To obtain a precise jaw calibration, we also made use of the portal imager rather than trusting the light field or using a film measurement. The mechanical precision of the gantry and MLC in RA delivery mode are monitored by the Snooker Cue test [54].

II.1. Detector evaluation

As field dimensions approach detector dimensions, the impact of the detector choice on the measurement outcome becomes critical. Much literature has already been attributed to this subject, especially when it comes to single detectors [43,44-46], and it is not the purpose of our work to present another in-depth characterisation of the different detectors available. However, we do aim to present a practical overview of the detectors and measurement methods in view

of their possible usefulness for dose calculation algorithm configuration and validation and for routine treatment QA. This benchmarking is performed entirely independent of the TPS.

0D: Point dose measurements

We have made use of the following PTW (Freiburg, Germany) detectors: the electron diode dE (TW60012), the stereotactic diode dSRS (TW60018), the photon diode dP (TW60008), the microDiamond μD (TN60019), the 3D PinPoint Pp3D (TN31016) and the Semiflex3D Sf3D (TN31021). An overview of the single detectors and some of their basic characteristics is given in the upper part of table 1, including their relevant dimensions and sensitivities. Although we refer to these measurements as '0D, point dose measurements', the 'point' inevitably encompasses the detector volume and therefore includes the dose-volume effect. Although the Octavius1500 and 1000SRS (both PTW, Freiburg, Germany) are two-dimensional arrays rather than single detectors, their presence in table 1 serves to characterise the individual ion chambers of the 2D composition. The Octavius1500 array consists of 1405 vented cubic ion chambers – of 0.44x0.44x0.3 cm^3 each –

mounted below a 0.5 cm polystyrene build-up layer and arranged on a 27x27 cm^2 surface area in a checkerboard pattern [55]. The 1000SRS array consists of 977 liquid-filled ion chambers - 0.23x0.23x0.05 cm^3 – distributed over a 11x11 cm^2 surface area: 400 ion chambers provide complete coverage of the inner 5x5 cm^2 surface area whereas the remaining chambers are distributed in a 0.5 cm center-to-center grid over the rest of the surface. [55]

A practical overview of the field size dependence was obtained by performing a series of dose measurements on the beam axis for collimator settings going from 1x1 to 5x5 cm^2 in combination with MLC (HDMLC) fields of dimensions 0.5x0.5 cm^2 to 3x3 cm^2. All data were acquired with 200 Monitor Units (MU), at depth = 8.5 cm and source-phantom distance SPD = 91.5 cm. We made use of a set of customized PMMA blocks of 5x10 cm^2 surface area and different thicknesses. A suitable insert was made for every detector. All data were acquired axially, i.e. with the beam axis along the detector axis, except for the Pp3D$_{rad}$ for which the beam incidence was perpendicular to the detector axis. The field size dependence of the arrays was measured in the same conditions by means of solid water plates (PTW) placed on top of the arrays. The daily output variation of the treatment unit as well as any possible deviations due to non-water equivalence of the PMMA were corrected through a cross-calibration factor based on the 5x5 open field measurement and the theoretically expected dose in water for all detectors. From the above measurements, the sensitivity (nC/Gy) could also be deduced and compared to the vendor specifications.

As mentioned above, we do not wish to take field size dependent correction factors into account and aim to assess the practical usability of the different detectors when not doing so. In order to present the results in an orderly fashion, we have decided upon the microDiamond as the reference detector. Although contradictory results [47,48,50,51,52] have been published regarding this detector's field size dependence for the smallest field dimensions (0.5 to 1 cm), a recent publication of Francescon et al. [49], re-confirms the original findings by Morales et al [51] and Chalky and Heyes [52] that microDiamond correction factors are within 1% down to a 7.6 x 7.7 mm MLC field size, and even within 1.5 % for cone sizes down

to 5 mm. (suggesting that the overresponse due to the mass-density effect is well-balanced by the volume averaging effect). We have therefore taken the doses measured by the microDiamond detector (and cross-calibrated to the 5x5 cm² field) as the reference values and have normalised all other detector data to these values in table 1 for comparison (thereby accepting a possible ~1-1.5% imprecision in the small(est) field data).

To assess the directional dependence, we made use of
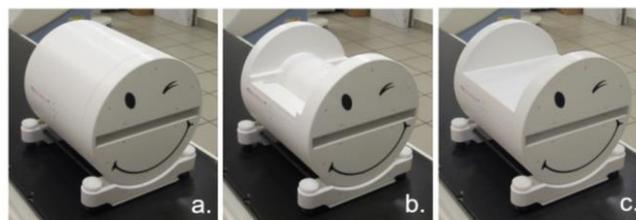
Figure 2: Modular Octavius4D measurement unit consisting of (a) the large diameter top (Oct4D_Maxi), (b) the SRS top (Oct4D_Mini) and (c) the flat top (Oct4D_Flat) which can all be used in combination with the 1000SRS 2D array.

Ruby, a geometric PMMA phantom developed for use in stereotactic treatment QA (figure 1a). All of Ruby's orthogonal cross-sections (transversal, coronal and sagittal) have an octagonal shape with sides of 6 cm, resulting in a total phantom thickness of 14.5 cm. Different detector inserts allow the use of all of the above single detectors. The directional dependence of the detectors can easily be assessed by irradiating Ruby with different combinations of gantry and couch rotations without the need for different MU calculations. All beam incidences orthogonal to the square 6x6 cm^2 surface areas have the same SPD: with the couch rotation set to 90 degrees, the gantry was positioned at 315, 0, 45 and 90 degrees (table 1 and figure 1b), respectively. All data were acquired with 128 MUs, delivering 1 Gy to the isocentre with a 3x3 cm^2 field size (which should be large enough to exclude an impact of the detector dimensions compared to the field size). The phantom and detector position were verified by means of the on-board imaging (orthogonal kV images or CBCT) prior to data acquisition and better than 0.5 mm in all directions. No directional dependence measurements were performed for the 2D arrays. The directional dependence of the Octavius1500 has been reported elsewhere and, like the 1000SRS, it should preferably be used only in a simple orthogonal setup or in the rotational Octavius4D unit [55].

1D & 2D*: water phantom scans and planar dose acquisition systems*

Depth dose measurements were performed in a MP3-M water phantom (PTW) for square fields of 1x1, 2x2, 3x3,4x4,10x10, 26x26 and 40x40 cm^2 at SPD = 95 cm with all of the above listed detectors. The detectors were positioned by means of the TrueFix (PTW Freiburg) system

Figure 1: a. Ruby, the small solid water phantom used with various point dose detectors. All orthogonal cross-sections of the phantom have an octagonal shape with 6 cm sides. b. The angular incidences (dashed arrows) used to assess the detector's directional dependence with the couch (or phantom) rotated by 90 degrees. The double-lined arrow indicates the gantry rotation.

to take their effective point of measurement into account. Both the water phantom and the gantry were carefully verified with a spirit level to ensure that the detector remained at the centre of the field at all times during the scan. The central position of the detector was furthermore confirmed at shallow and large depth by means of two orthogonal profile scans acquired with small step size (1 mm) around the penumbra region. During the depth dose scans, the acquired signal was not divided by the signal of a reference chamber because the physical presence of the latter would risk having an impact on the measurement for the smallest field sizes. This approach is justified because of the stability of the linac's dose rate output during data acquisition. Furthermore, the measurement range was not adjusted in between scans with the same detector so the signal could be converted to the dose for a 200MU delivery through cross-calibration to the 10x10 cm^2 measurement.

To compare the dosimetric precision (absolute dose level and geometric resolution) with which the different point detectors can measure profiles, scans were acquired in the water phantom for a single static artificial MLC field (MLC120), containing 8 cm long open field strips of different widths (0.5, 1.0 and 1.5 cm wide, corresponding to 1, 2 and 3 adjacent open leaf pairs, respectively), alternating with 1 cm wide strips of 2 closed leaves. The field size defined by the jaws was 10x10 cm^2. Scans were performed perpendicular to the MLC leaves at SPD = 95 cm and depths 5, 10 and 15 cm. Similar to the depth dose data, scans were converted to the absolute dose for a 200 MU delivery through cross-calibration of the detector signal with an open 10x10 cm^2 field. The same MLC pattern was also measured with the 1000SRS 2D array in solid water (200 MU). At each depth, the 1000SRS array was cross-calibrated to the dose obtained for a 5x5 cm^2 open field in water (100 MU) at the maximum dose rate (600 MU/min for 6MV). As an additional planar measurement system, we included the MV portal imager (aS1000, Varian) and delivered the above static MLC field (200 MU) to the aS1000 MV imager using the integrated image acquisition mode. The imager panel was calibrated for this dosimetric acquisition mode using the profile correction files from the preconfigured package [57].

3D: volumetric dose reconstruction in the modular Octavius4D rotational unit

The modular Octavius4D (Oct4D) measurement system provides a 3D dose reconstruction that is entirely measurement-based and independent of the information contained in the TPS dicom dose (or dicom plan) file. The phantom consists of a rotational base in which a variety of 2D arrays can be inserted and upon which three different tops can be mounted, depending on the purpose of the measurement and the type of treatment (figure 2). For standard treatment localisations, the Octavius729 or Octavius1500 array would be used in combination with the standard top, creating a 32 cm diameter cylinder as shown in figure 2a (Oct4D_Maxi) [55]. For stereotactic treatments, the SRS top generates a 17 cm diameter cylinder (figure 2b),

to be used along with the 1000SRS (Oct4D_Mini). Although the 1000SRS array can also be used in the standard setup, the SRS top corresponds to a more realistic diameter for e.g. intracranial stereotactic treatments. The third, flat solid water top (figure 2c, Oct4D_Flat) is not designed to be used for 3D dosimetry but for treatment unit QA. It can, however, also be useful to measure the projection of the treatment delivery into a single plane during arc treatment, analogous to the portal image acquisition but in a 5cm deep water equivalent setup rather than in an amorphous silicon environment. The inclinometer mounted on the gantry ensures that the rotation unit always rotates along with the gantry, thus keeping the 2D array perpendicular to the beam axis at all times.

The measured dose as a function of gantry angle is stored in the measurement file every 200ms. Upon loading this file in the Verisoft software, the 3D dose in a homogeneous cylindrical phantom is reconstructed: for every stored gantry angle, the 2D measurement data are extrapolated to the rest of the cylinder by applying a percentage depth dose (PDD) curve through every measurement point. The total 3D dose is then reconstructed as the sum of these individual contributions and linearly interpolated to a user specified dose grid. For the stereotactic dose reconstruction, we have set the grid to 1 mm (instead of the default 2.5 mm). The software decides on the field size for which to select the PDD based on the effective surface of the array irradiated for every gantry angle. The set of PDD curves needed for this reconstruction should be acquired beforehand in a water phantom. As we have been routinely performing QA of RA treatments on the previous (non-modular) Octavius4D model (diameter 32 cm), such a set had long been measured in our department at SPD = 85 cm with an ionisation chamber (0.125 cm^3 Semiflex, PTW) for field sizes ranging from 27x27 to 3x3 cm^2 and subsequently extrapolated down to a virtual 0x0 cm^2 field size to cover all field sizes that could possibly be needed during the reconstruction process. This PDD set will be further referred to as PDD$_{85}$. With the possibility of using both the standard as well as the SRS top in the modular system, however, it needs to be verified whether the PDD$_{85}$ set can be used for both phantom compositions and whether the theoretical extrapolation below 3x3 cm^2 does not introduce deviations for stereotactic treatment fields. We have therefore acquired additional PDDs in the water phantom at SPD= 91.5 cm and SPD = 84 cm, i.e. at the exact SPDs of the Oct4D_Mini and the Oct4D_Maxi setup, respectively. We have measured the PDDs of simple open fields (27x27 down to 1x1 cm^2) and of the stereotactic MLC fields listed in table 1. The Sf3D was used for effective field openings above 5x5 cm^2 while all smaller dimensions where measured with the dSRS. The open field PDDs at SPD 91.5 cm were also used to generate alternative PDD sets for Verisoft (PDD$_{91.5}$). The small fields (X, Y or MLC ≤ 5 cm) were subsequently measured with the 1000SRS array in the Oct4D_Mini and Oct4D_Maxi. The 3D doses were reconstructed in Verisoft with the

relative electron density of the Oct4D material set to 1.00 and using both PDD sets (PDD_{85} and $PDD_{91.5}$) on all data. The PDD along the beam axis of the reconstructed doses was then exported from Verisoft and compared to the PDDs measured in the water phantom at the same SPD. As the Verisoft 3D dose reconstruction has no prior knowledge of the actual collimator or MLC position but selects the PDD solely based on the effectively measured field dimensions, these test fields allow an assessment of the validity of this approach by comparing the truly measured PDD with the Verisoft reconstructed PDD, for both open and MLC fields. (Although the water phantom PDDs were acquired with a flat water surface instead of the curved shape of the cylindrical phantom, the consequences of this geometric discrepancy are negligible when focussing on small field sizes, for which the curve of the cylindrical surface is too small to noticeably impact the shape of the depth dose on the beam axis.)

Finally, a number of simple rotational test deliveries were created around spherical target structures of 1.0, 1.5 and 3.0 cm in diameter. Conformal arc plans were generated by adjusting the MLC and jaws tightly around these targets, bearing in mind minimum jaw settings of 1x1 cm^2. In addition to the conformal arcs, RA plans were created on each of the three targets with a single arc per plan. To facilitate interpretation of the data, the collimator was kept at 0°. All of these arcs were measured with the 1000SRS array in both Oct_Mini and Oct_Maxi. The absolute dose reconstructed by Verisoft at isocentre was compared to the absolute dose measurement performed with the Pp3D and µD inserted into the rotational phantom by means of the dedicated solid water insert. Both the 1000SRS and the point detectors were cross-calibrated to the theoretical dose of a 5x5 cm^2 field at the center of a water equivalent cylinder of 32 cm or 17 cm diameter, respectively.

II.2. Dose calculation algorithm configuration and validation

II.2.1. Algorithm configuration

Upon configuring a dose calculation algorithm with beam data measured in a water phantom, it is not only important to know the characteristics of the detector used for these acquisitions, but also to understand which aspects of the data are of importance to the configuration of the calculation model and which are not. In short, it is often most beneficial to understand the process of the algorithm configuration before starting with the actual beam data acquisition.

The AAA and AXB dose calculation algorithms require the same basic beam data input for configuration: a series of open field PDDs, profiles of these open fields at five different depths, diagonal profiles of the largest field size at the same five different depths and output factor measurements (performed at a depth beyond d_{max}). Although a minimum amount of data needs to be provided, the choice of field sizes is pretty much left up to the user, as long as the largest field is included. For standard algorithm configuration, users usually measure beam data for fields ranging between 3x3 cm^2 and 40x40 cm^2. The purpose of the configuration module is to characterize the phase space of the photon beam. Once the modelling of the parameters describing this phase space is complete, the measured PDDs and profiles will no longer be used during the actual dose calculations. Only the output factors are still involved in the monitor unit (MU) calculation.

In theory, if one wishes to calculate small field dosimetry with the AAA or AXB algorithm, one can simply do so by using the 'standard' algorithm configuration without including any additional small field data into the beam configuration data set: the algorithm will calculate depth doses and profiles according to the configured phase space and extrapolate MUs to smaller field sizes than the ones specified in the output factor table. As especially the latter is clearly not advisable, we present an overview of the (additional) measurements that were performed to include small field dosimetry in the AAA and AXB configuration in order to investigate their respective impact on the precision of the stereotactic dose calculation compared to the 'standard' configuration

Small field depth doses and profiles:

During beam configuration, Eclipse will ignore PDD measurements for field sizes below 2x2 cm^2 based on the assumption that PDDs for very small field sizes are easily subject to measurement imprecision and therefore more likely to deteriorate rather than improve the phase space modelling . It is therefore a waste of effort to try and carefully measure the 1x1 cm^2 PDD for beam configuration. A similar reasoning holds for the small field profiles. Although it would be tempting to measure the field profiles with a high resolution detector to accurately reproduce the penumbra at the field edge, this sharp penumbra gradient is not used in the phase space modelling, precisely because of its known detector dependency. It is more important to have a reliable dose measurement of the profile tails under the jaws than it is to have a sharp penumbra. For all of the above reasons, we made use of the Sf3D ion chamber for the complete basic beam data acquisition. As an ion chamber it produces a reliable dose measurement under the jaws and because it can measure PDDs down to 2x2 cm^2, all data can be acquired with a single detector. The only other detector that is equally versatile would be the µD, but as the latter has a lower sensitivity than the Sf3D, data acquisition will have to be slowed down or yield a smaller signal-to-noise ratio than the Sf3D.

Small field output factors:

In contrast to the small field depth dose and profile measurements, the output factors have a more visible impact on the configured data. They result in the calculation of additional collimator backscatter factors and directly impact the MU calculation for the small field dimensions. Before

the acquisition of the small field output factors (dimensions < 3 cm), the calibration of the jaws was carefully verified for all treatment units and adjusted where necessary to obtain the highest possible positional accuracy (< 0.5 mm) for each individual jaw. Output factors were measured in isocentric conditions at SPD = 95 cm and depth = 5 cm with the Sf3D for field dimensions down to 3 cm (X or Y). Additional data were acquired with the dE, dSRS and μD for field dimensions between 1 and 3 cm, with additional measurement points for the 4x4 and 5x5 cm^2 fields to confirm a seamless merge of both data sets. The overlapping measurements for the X = 3 cm or Y = 3 cm fields provide an additional check.

Both dose calculation algorithms (AAA and AXB) were configured with the above acquired input data, the only difference being the size of the point source set to 0 mm for AAA and 1 mm for AXB, according to Varian recommendations [42,58].

MLC parameterisation:
The MLC parameters were derived according to our standard method for IMRT or RA implementation, making use of the Octavius1500 2D array in solid water (SPD = 95 cm, depth = 5 cm), measuring four different fields: first a static open field with the same collimator settings as the subsequent MLC fields (12x24 cm^2 for the 120MLC, 12x20 cm^2 for the HDMLC), second a static field with closed MLC to derive the overall leaf transmission, third a dynamic sweeping gap field (with a gap of 5 mm) to derive the dosimetric leaf gap (DLG) parameter modelling the rounded leaf tips and fourth a dynamic delivery in the shape of a chair [59] to make sure we have a consistent set of MLC parameters and have not compensated possible errors in the transmission measurement by introducing a suboptimal value for the DLG. Although the tongue and groove effect of the MLC is taken into account in the calculation in a similar fashion as the DLG, albeit in the direction perpendicular to the MLC leaves, this is a parameter that can not currently be adjusted by the user and therefore requires no configuration measurements. Even so, an additional test series was performed to assess the dosimetric precision of its modelling in Eclipse v11. They are therefore described in the below paragraph concerning the algorithm validation rather than configuration.

II.2.2. Algorithm validation

Although the AAA and AXB algorithms need only few additional data in order to be configured for small field dosimetry calculations, careful validation is advisory as the small field dose calculation pushes the algorithm to the limits.

In order to validate both algorithms, we have reused the (MLC) fields (static and dynamic) for which data had already been acquired during the detector validation, adding more field sizes (with and without MLC) wherever

desirable. Whereas measurements for the detector characterisation could be performed on either the NovalisTX or the Clinacs, for the dose calculation validation, similar datasets were always acquired on all treatment units.

0D: point dose validation:
The measurements in the solid water blocks (SPD = 91.5 cm, depth = 8.5 cm) were calculated in Eclipse on an artificial water phantom with both AAA and AXB. The calculation resolution was set to 2.5 mm ($AAA_{res2.5}$ and $AXB_{res2.5}$) and to 1.0 mm ($AAA_{res1.0}$ and $AXB_{res1.0}$). Measurements were performed with the dE, dSRS and μD detector.

1D & 2D: dose profiles and planar dose validation:
The water phantom depth dose data acquired for the validation of the Oct4D dose reconstruction process were also used for the validation of AAA and AXB. Calculations were performed with 200 MU in the same conditions as the measurements, i.e. on a rectangular phantom at SPD = 91.5 and 84 cm. Similarly, dose profiles were calculated for the MLC field containing the narrow strips of opened and closed leaves (SPD = 95 cm, d = 5, 10, 15 cm, 200 MU) and compared to the measurements. In addition, to allow an indirect but easy evaluation of the changes in the photon fluence as a function of calculation resolution, portal dose images were predicted from the four calculated plans ($AXB_{res1.0}$, $AAA_{res1.0}$, $AXB_{res2.5}$ and $AAA_{res2.5}$), providing us with images based on photon fluences with resolutions 0.5, 1.0, 1.25 and 2.5 mm, respectively. (The portal dose prediction algorithm had been configured with the beam data from the preconfigured package.) These were compared to each other as well as to the portal image acquired with the aS1000 MV imager panel.

The 1000SRS and aS1000 2D detectors are also practical for the validation of the Eclipse MLC modelling. The MLC transmission and DLG parameter values were optimized during the configuration to achieve good agreement between dose calculation and measurement. The tongue and groove effect, however, is subjected to further investigation. Maximal tongue and groove effect was achieved by creating a dynamic treatment field consisting of two complementary static MLC segments. The first segment (100 MU) has all impair leaf pairs opened to form a 5 cm gap while all other leaf pairs remain closed under the jaws. In the second segment (100 MU), the impair leaves are closed while the pair leaves create the 5 cm openings. This dynamic MLC was used in combination with different jaw settings to investigate the tongue and groove for all leaf widths present in both MLC types. The portal imager was used to provide a high-resolution image of the tongue and groove pattern and compare it to the dosimetric image that was predicted based on the photon fluence calculated by Eclipse. For the portal imager, jaws were set sufficiently large to include all leaf widths within a single measurement. The predicted image was calculated from the $AXB_{res1.0}$ dose calculation,

corresponding to a 0.5 mm internal fluence resolution. Data were also acquired with the high resolution 1000SRS array in between solid water plates (SPD = 95 cm, depth = 5cm). To make full use of the high detector density in the central part of the array, a symmetric 5x5 jaw opening allows measurement of the tongue and groove pattern for the central leaves (2.5 mm (HDMLC) and 5 mm (120MLC), respectively). The array was then moved longitudinally to measure another 5x5 field, this time with highly asymmetric jaw settings to also include the outer leaves (5 mm (HDMLC) and 10 mm (120MLC), respectively). Measurements were compared to the corresponding calculations.

3D: volumetric dose validation:

As the 3D dose reconstructions obtained with the Oct4D_Mini and Oct4D_Maxi phantom were first independently validated by means of water phantom (for the static gantry) and point dose measurements (for the arc plans), these can now be used to verify the accuracy of the 3D dose calculation algorithms. Both the static gantry and the rotational plans were recalculated with $AAA_{res1.0}$ and $AXB_{res1.0}$ and dose distributions were exported for comparison in the Verisoft software.

II.3. Patient QA

Having benchmarked the precision with which different measurement methods can be relied upon and the dosimetric accuracy that can be expected from the TPS in simple plan deliveries, we can commence the validation of real stereotactic RA patient treatments.

The patient plans encompass a variety of treatment localisations. Single lesions were mostly treated with the isocentre placed within the lesion. RA optimizations were performed either with the commonly used non-coplanar arc setup (with multiple couch rotations) or, if possible, with coplanar or slightly non-coplanar arc delivery. Multiple lesions were either treated with multiple isocentres (in which case they can simply be regarded as multiple single lesion treatments when it comes to treatment QA) or with a single isocentre. In the latter case, if lesions are well separated, we treat both lesions with separate arcs, albeit all with the same isocentre. If they are closely spaced, we optimized on both volumes in the same arc, but add additional arcs to allow for more modulation. The plan quality that can be obtained with these different beam geometries depends on the size and location of the lesion(s) but as this is not the subject of this manuscript, it will not be elaborated on. However, as we do use all of the above setups in clinical routine, the QA protocol needs to be able to handle all of them. We have therefore first prepared two test patients on the Clinac iX, one with a single lesion (1Meta) (diameter ~ 1.5 cm) and one with two separate lesions (2Meta) of different sizes (diameters ~ 2 and 1 cm, respectively) but relatively closely spaced (center-to-center

distance of ~ 3 cm). Both cases were planned with three different treatment approaches regarding couch movement: firstly, the more traditional, radically non-coplanar setup was used with multiple couch rotations, secondly a plan was optimized for a coplanar arc geometry and lastly, a nearly-coplanar setup (with couch rotations set at 10 and 350 degrees) was used to avoid concentrating the dose outside of the target into a single cross-section of the brain whilst still minimizing couch rotation. These six treatment plans were validated in-depth with the following measurement methods:

0D) μD and Pp3D in Ruby: for every lesion, the phantom position was optimized to have the detector at the centre of the lesion. To avoid mistakes and minimize inaccuracies during set-up, a CBCT was acquired (without couch rotation) for every localisation and the phantom position was adjusted accordingly. Subsequently, for every point dose measurement, the entire treatment plan was delivered preserving the original couch rotations. Once positioned, no more image-guided adjustments to the phantom were made for the different couch rotations. Dosimetric deviations due to a possible imprecision in the couch movement are therefore inherently included in the measurement.

3D) 1000SRS in Oct4D_Maxi and Oct4D_Mini: a verification plan is generated in Eclipse to calculate the expected dose in the Oct4D phantom ($AAA_{res1.0}$ and $AXB_{res1.0}$). For both the measurement and calculation, couch rotations are set to zero. 3D dose distributions are exported for the total dose as well as for the individual arcs.

In addition, all routine stereotactic patients treated on the NovalisTX were verified with the 1000SRS/Oct4D_Maxi until the modular Octavius became available and from then on verification has been carried out with the 1000SRS/Oct4D_Mini combination instead. As AXB is not yet available for routine purposes on the NovalisTX, all of these plan verifications were calculated with $AAA_{res1.0}$. Point dose measurements were carried out occasionally.

To analyze the 3D dose information, the standard gamma criteria accepting 3% dose differences (local (%L) or global (%G)) in combination with a 3 mm distance to agreement (DTA) are deemed inappropriate for stereotactic treatments. While we can be more tolerant on the absolute dose level in the high dose area, we aim to be more precise regarding the location of the dose peak. We have therefore performed all 3D gamma analysis (γ_{3D}) with a DTA of 1 mm while varying the local dose criterion. Volumetric gamma evaluation scores were obtained for different isodose levels by means of the volumetric gamma analysis tool in Verisoft, representing the percentage of points that pass the criteria within the volume delineated by the given isodose level. To allow focus on the high dose area, as levels of interest, we have opted for the 90%, 70% and 50% isodose volumes. The local dose criterion was varied between 3% and 5% to

investigate if – and at which tolerance level - near-perfect ($\geq$ 99%) pass rates (PR) could be achieved.

III. RESULTS

Firstly and importantly, after careful recalibration of the jaws, submillimeter precision was achieved for all mechanical components on all treatment units when evaluated in static mode. In RA treatment mode, the successful use of the Snooker Cue test assured a dynamic rotational precision within 1 degree, even under extreme acceleration and deceleration conditions. An appropriate procedure was implemented to ensure that these mechanical precisions are maintained over time.

III.1. Detector evaluation

0D: Point dose measurements

Table 1 provides an overview of the dosimetric characteristics for the different detectors relevant to stereotactic dose measurements. To assess the field size dependence, the data were first normalized to the 5x5 open field measurement for each detector. The microDiamond measurement was then chosen as the reference [49] and all measured output factors were divided by the one measured with the µD. The diodes have the smallest radii (0.06 cm)

and the highest sensitivity, making them all well suited for dose measurements down to dimensions of 1 cm in orthogonal measurement conditions. Even for smallest measured field dimension of 0.5x0.5 cm², deviations are only ~ 3%. The single ion chambers can all be used with good accuracy down to 2x2 cm^2, but start to diverge by 4 to 50 % below. In spite of its dimensions similar to the Pp3D, the central chamber of the 1000SRS proves to be a good dose detector down to the smallest field size as well. The vented ion chambers of the Oct1500, however, cannot be relied upon for accurate dose measurements of field sizes below 3cm.

From table 1, it is furthermore apparent that apart from the Pp3D and Sf3D ion chambers, only the µD shows a directional independence. The diodes all measure a considerably lower signal when not irradiated axially.

Although the sensitivities widely differ between the different detectors, this did not really affect the outcome in table 1 as all data could simply be acquired with high enough dose to obtain a good signal to noise ratio.

1D & 2D: water phantom scans and planar dose acquisition systems

To compare the measured depth dose data between different detectors, figure 3 shows a plot of the relative difference between the different PDDs. All PDDs were first normalized to a depth of 5 cm and then divided by the supposed reference PDD. For the small field dimensions (< 3 cm), we opted for the dSRS as the baseline, whereas for
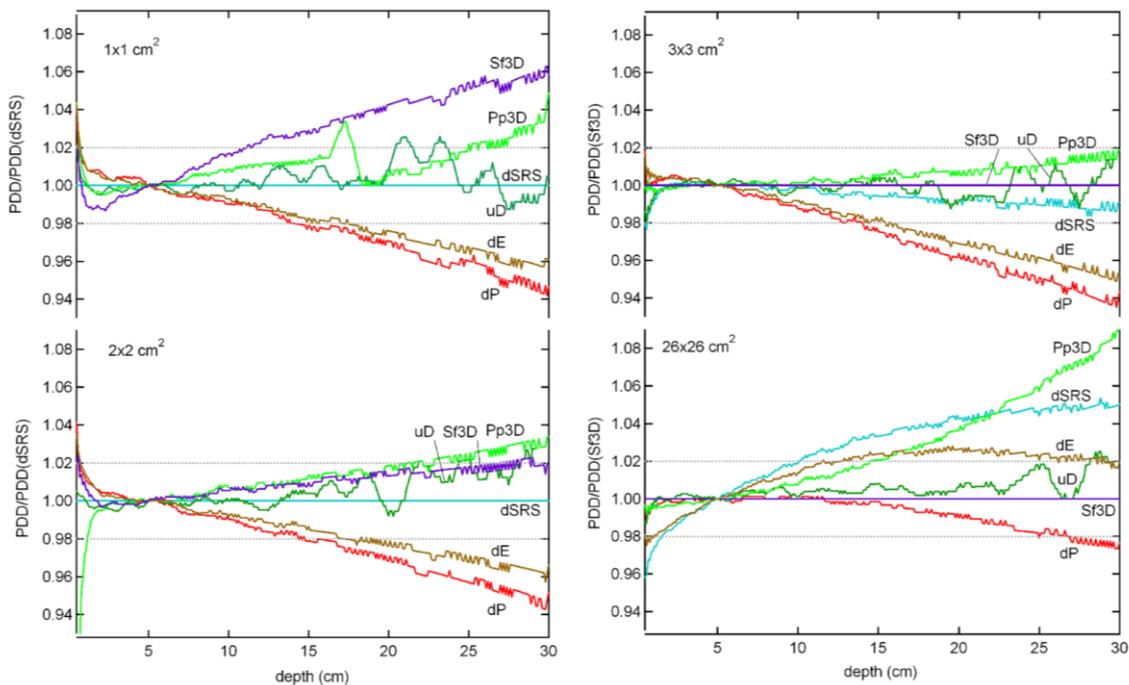
Figure 3: Comparison between depth dose curve measurements using the different detectors listed in table 1. For field sizes 1x1 and 2x2 cm^2(graphs on the left side), the acquired PDDs are normalized to the dSRS PDD. For the larger field sizes (graphs on the right), data are normalized to the Sf3D measurement. The horizontal, dotted lines indicate the 2% interval around the reference PDD.
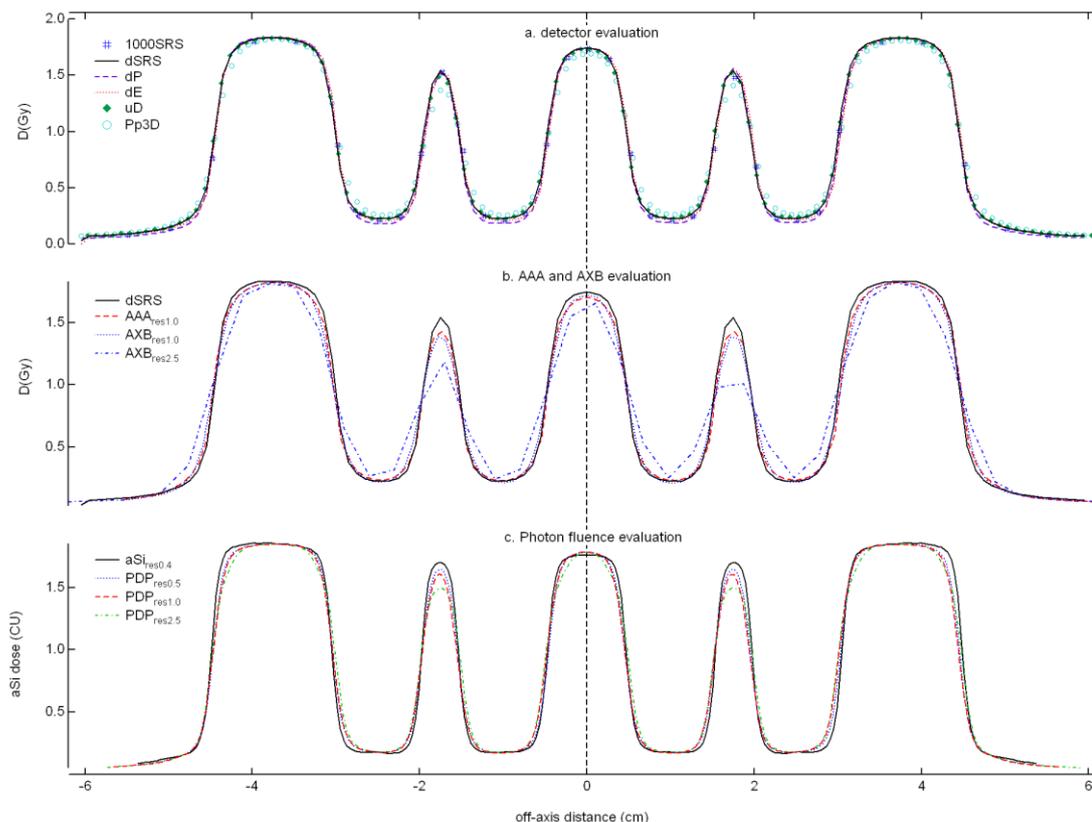
Figure 4: Profiles for the MLC striped field: (a) detector evaluation: profiles measured at SPD = 95, depth = 5cm with different high resolution point dose detectors: the lines correspond to the diode measurements (dSRS: solid black, dP: dashed mauve, dE:dotted red) the µD (solid green diamonds), the Pp3D (open cyan circles). A line profile was also extracted from the 1000SRS planar measurement (dark blue hashtags). (b) AAA and AXB evaluation: comparison between reference measurement (dSRS, black solid line) and different dose calculations: resulsts for $AAA_{res1.0}$ and $AXB_{res1.0}$ are similar, displaying a slightly too broad penumbra and too low dose in the narrow peaks. On the central axis, the $AAA_{res1.0}$ dose calculation is 1% lower than the corresponding AXB dose calculation. Dose calculations with 2.5 mm resolution ($AAA_{res2.5}$ not shown but similar to $AXB_{res2.5}$) are drastically too broad. (c) Photon fluence evaluation: profile comparison between portal dose images predicted with different fluence resolution showing the same gradual decline of the peak in the narrowest strips as well as the increased broadening of the penumbra. The measured dosimetric image is also displayed (solid black line) and shows sharper penumbra and higher peaks.

the larger dimensions (≥ 3cm), all data are displayed relative to the Sf3D acquisition. The dotted horizontal lines indicate the 2% interval above and below these baseline PDDs. The dE and dP come out as the least suitable for overall small field PDD acquisition, deviating by more than 2% at larger depths (>15 cm). The µD appears to be the most versatile detector, agreeing with the baseline PDDs within 2% over the whole field size range. However, the numerous bumps and valleys are a reflection of the noisier aspect of the data acquired with this detector, in spite of the considerably longer acquisition times used. The ion chamber capable of accurately measuring small field PDDs down to 1x1 cm^2 is the Pp3D, but this detector is suboptimal for larger fields. The Sf3D demonstrate nearly equally versatile behaviour as the µD, but with better signal-to-noise ratio: this detector is suitable for all field sizes, with the exception of the smallest 1x1 cm^2 field.

The impact of the detector resolution can be observed in the profiles acquired for the MLC-striped field shown in figure 4a. All diodes and the µD have a sufficiently small resolution to accurately reproduce the dose peaks corresponding to the open MLC strips. The 0.145 cm diameter of the Pp3D has the expected broadening effect on the profiles that can mostly be observed from the decrease in the 0.5 cm and 1 cm wide dose peaks, accompanied by the increase of the low dose measured in between the peaks. In spite of its similar ion chamber dimensions, the 1000SRS, however, does not display this broadening effect and demonstrates behavior expected of a spatial resolution of the order of 1 mm rather than 2.4 mm. The dose maxima or the narrow peaks also agree very well with the ones observed with the diodes. In the valleys shielded by the MLC, dP consistently reports the lowest dose whereas the Pp3D overestimates the dose. The other detectors all show good agreement, with the µD and dSRS being ever so slightly higher than the dE and the 1000SRS.

The aSi acquired images cannot be compared to water phantom measurements as they do not provide dose to water and are therefore not added to figure 4a. Without an image prediction algorithm, they can basically only be used to verify the geometry of the field and MLC outline. They are therefore only presented in figure 4c and will be evaluated in more detail during the TPS validation.

3D: volumetric dose reconstruction in the modular Octavius4D rotational unit

Figure 5 displays a selection of small (MLC) field depth dose curves as measured in the water phantom and as extracted from the 3D dose reconstructed by the Verisoft software. The Oct4D data in the upper half of the graph are obtained from measurements in the Oct4D_Maxi setup, while the lower half corresponds to Oct4D_Mini. Both were reconstructed with the two PDD reference sets. Upon close inspection, we observe that the 3D dose reconstruction along the beam axis is most accurately reproduced when a PDD set is used that was acquired with a SPD similar to the phantom setup: the Oct4D_Maxi dose reconstruction has a near-perfect agreement with the water phantom data when the PDD_{85} is used while slight deviations in the slope of the depth dose are observed when applying the $PDD_{91.5}$

reference set. The inverse is true for Oct4D_Mini for which the $PDD_{91.5}$ reconstructed data are superior. However, it needs to be said that the observed deviations with the non-corresponding PDD sets are small and only visible for off-isocentre distances larger than 2.5 cm, i.e. outside of the 3D volume that will be reconstructed from the ion chamber data in the central part of the detector. Furthermore, the slightly different slope will be partially annihilated in the 3D reconstruction of rotational delivery. Also noteworthy: although the PDD_{85} reference data-set was created with extrapolated rather than measured PDDs below 3x3 cm^2, these extrapolated data seem to yield equally good small field dose reconstruction as the $PDD_{91.5}$ for which depth doses were actually measured down to 1x1 cm^2.

For the arc treatments measured with the 1000SRS no difference could be distinguished between the dose reconstructions with the different PDD sets. The reconstructions shown in figure 6 have been generated with PDD_{85}. As can be seen, all Oct4D_Maxi measurements report an isocentric dose that agrees within 1% with the µD measurement. The Pp3D measures an equally good agreement for the conformal arcs on the 1.5 cm (figure 6b) and 3.0 cm (not shown) target, but underestimates the dose
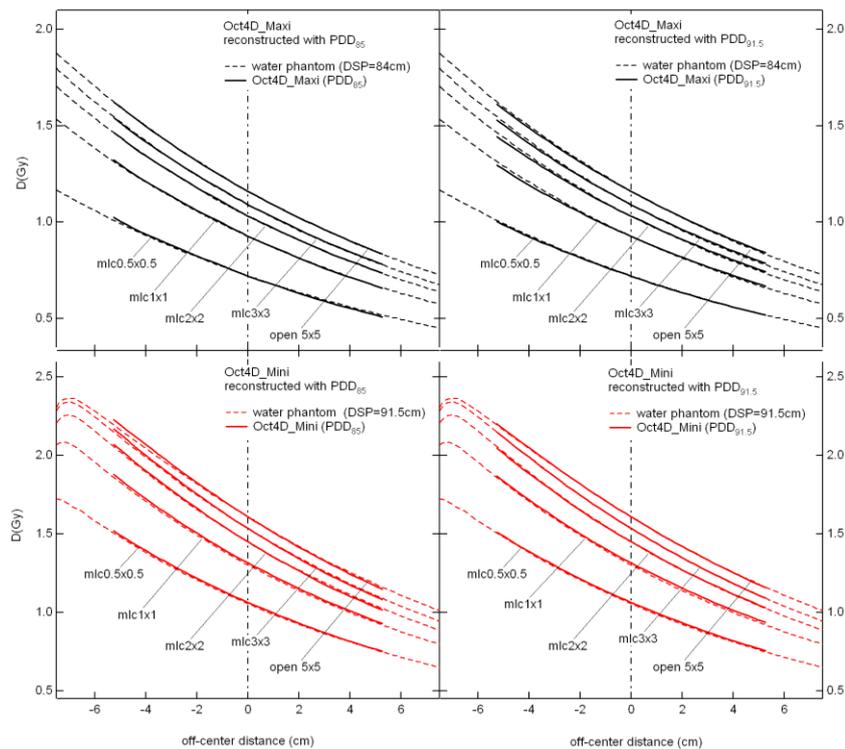
Figure 5: Comparison between water phantom measured PDDs and Oct4D reconstructed PDDs for Oct4D_Maxi and Oct4D_Mini. Small field (open and MLC) PDDS as measured in the water phantom are represented by the dashed lines at SPD = 84 cm (black, upper graphs) and SPD = 91.5 cm (red, lower graphs). The solid lines represent the PDDs extracted from the Oct4D_Maxi (upper graphs) and Oct4D_Mini (lower graphs) dose reconstruction using two different PDD reference sets. Graphs on the left were reconstructed with the PDD_{85}, graphs on the right were reconstructed based on the $PDD_{91.5}$. Comparison shows that best results are obtained when a PDD set adapted to the actual phantom SPD is used.
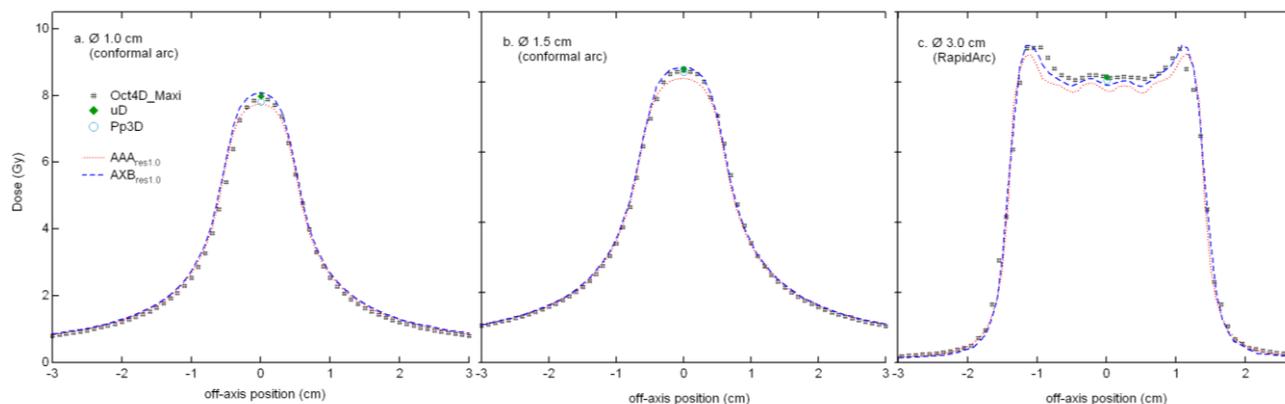
Figure 6: Results on the conformal and RA plans made on simple spherical targets of (a) 1.0 cm, (b) 1.5 cm and (c) 3.0 cm diameter. Symbols represent the different measurements: black hash tags are profiles extracted from the Oct4D_Maxi dose reconstruction. Coronal cross-sections indicating the position of the extracted profile are shown in the insets. Point dose measurements with the μD (green, solid diamonds) and Pp3D (light blue, open circles) at the isocentre are also displayed. Red dotted lines and dashed blue lines represent the AAA$_{res1.0}$ and AXB$_{res1.0}$ calculations, respectively.

of the smallest PTV by 3% (figure 6a). Similar results are obtained when comparing the RA measurement at isocentre between the μD,Pp3D and Oct4D_Maxi. The RA plan on the largest target is shown as an example in figure 6c.

III.2. Dose calculation algorithm configuration and validation

3.2.1. Algorithm configuration

Both dose calculation algorithms were successfully configured. Compared to the original, 'large field' algorithm configuration, no significant difference was observed in the calculated phase space parameters, apart from the fact that both the output factor table and the collimator backscatter factors now contain values down to a 1x1 cm^2 field size.

For the 120MLC, the leaf transmission was set to 1.5 %, providing an acceptable compromise of the overall transmission for both the 0.5 and 1.0 cm wide MLC leaves. The sweeping gap measurement provided a fairly flat total dose delivery and agreed well with TPS calculation for a DLG set to 0.14 cm. For the HDMLC, however, the overall leaf transmission is higher for the inner leaf area (1.25 %) than for the outer leaf area (1.1 %). As the inner leaves are predominantly used during (stereotactic) treatments, we have set the leaf transmission to 1.25 %. The DLG value was set to 0.09 cm to obtain good agreement between measured and calculated data for the central leaves. The results on the tongue and groove modeling are presented in figure 7. The portal images (upper graphs) indicate a promisingly good overall agreement between the measured and calculated photon fluence for both MLC types, as long as the calculation is performed with a sufficiently high resolution. This satisfactory agreement is also found in the comparison between the 1000SRS measurements and the dose calculations for the 120MLC, for the central (middle

graph of figure 7a) as well as for the outside leaves (bottom graph of figure 7a) as dose measurements and calculations intertwine. For the inner leaves of the HDMLC, however, the calculated dose level is systematically lower than the measurement (middle graph of figure 7b). Although the individual leaf positions could still be distinguished in the predicted portal dose image, this is no longer so for the in-phantom dose calculation. The Eclipse dose calculation grid not only smoothens out the tongue and groove effect, it also overestimates its impact on the dose reduction. The off-axis measurement on the HDMLC confirms the above findings (lower graph of figure 7b): while the overall dose level below the 2.5 mm leaves is ~ 7% too low, the 5 mm leaves are more adequately modeled as measurement and calculation overlap again.

3.2.2. Algorithm validation

0D: point dose validation:

Although many more jaw/MLC combinations were measured and calculated for the algorithm validation, table 2 shows a representative selection of the data as a function of field size, algorithm and calculation resolution. A lot can be learned from careful inspection of these simple datapoints. Firstly and most clearly, the absolute calculations for the small fields (≤ 2x2 cm^2) are unacceptable when calculated with a 2.5 mm calculation grid, regardless of the algorithm. Results for this calculation grid are only shown for the HDMLC, but were comparably poor for the 120MLC. For the 1 mm dose resolution, however, it can be observed that agreement between measurement and calculation is better for data obtained on the Clinac iX than on the NovalisTX: the field dimensions below 2x2 cm^2 show a ~ 2% larger deviation on the NovalisTX than on the Clinac iX. To investigate whether this should be attributed to a difference in the algorithm configuration or to the different MLC types, the datapoints for the HDMLC were recalculated with the
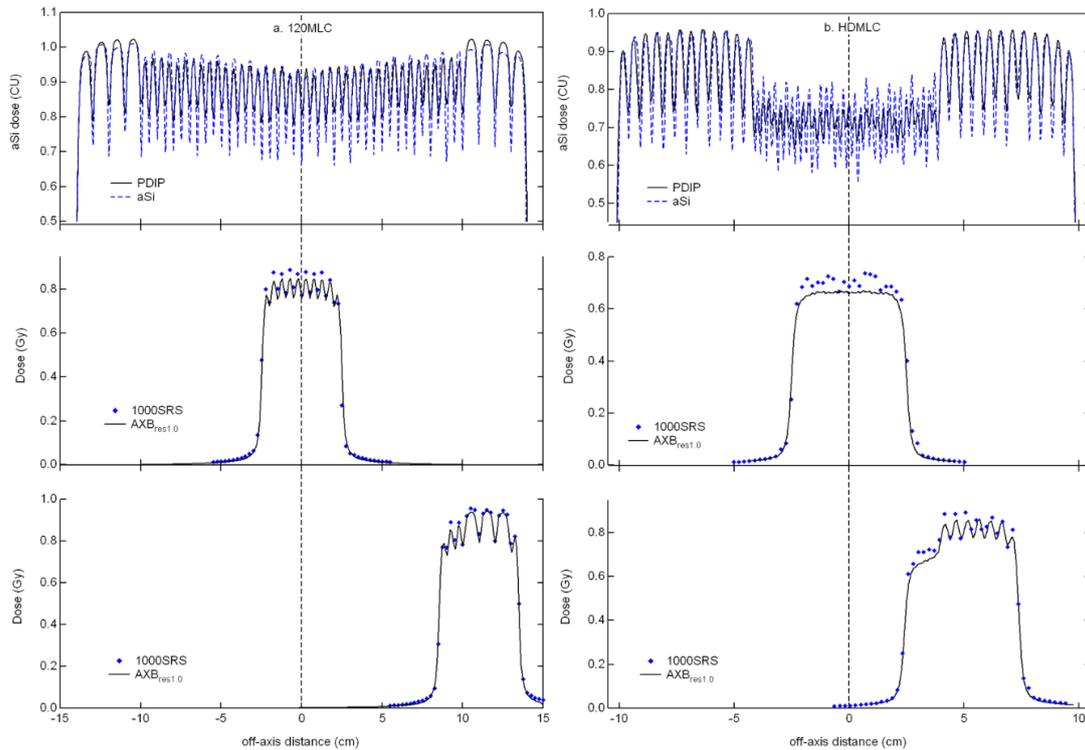
Figure 7: Evaluation of the tongue and groove model in Eclipse for the 120MLC (a. graphs on the left) and HDMLC (b. graphs on the right) by means of the step and shoot MLC plan with alternating leaf pair openings. Profiles perpendicular to the leaf movement are extracted from the planar measurements. The upper graphs display the high-resolution aS1000 (aSi) portal dose measurement (dashed blue line) and the portal dose predicted image (solid black line) based on the photon fluence as modeled by Eclipse during the $AXB_{res1.0}$ dose calculation. The middle graphs show the 1000SRS measurement (solid blue diamonds) for a central $5x5cm^2$ field opening - including only the central leaves into the results - while the lower graphs have a highly asymmetric 5x5 field-of-view to include both MLC widths for every MLC type. Dose calculations are shown for $AXB_{res1.0}$ (solid black lines).

Clinac iX algorithm configuration. (Although these treatment units do not officially have matched beam characteristics, when comparing their depth doses, profiles and output factor measurements in water, they appear near-identical, apart from a small (< 2%) difference in the field flatness, visible only in the profiles of the largest field sizes.) When recalculated with the Clinac iX beam data (not shown), agreement between measured and calculated dose is very similar for both MLC types, confirming that the inferior outcome on the NovalisTX in table 2 is beam data rather than MLC related. Best results were obtained with $AXB_{res1.0}$ on the Clinac iX: all point dose calculations

agreed within 2.5 % with the corresponding measurement. While results for $AXB_{res1.0}$ are slightly better than for $AAA_{res1.0}$ on the Clinac iX , the latter showing agreement within ~5 % for the smallest field sizes, this improvement is less systematic for the NovalisTX. Overall results on the NovalisTX are very good down to dimensions of 2 cm, below which deviations rise from ~ 5 % for the 1x1 cm^2 field to ~ 10% for the smallest 0.5x0.5 cm^2 field opening. To investigate whether the differences between AAA and AXB could be related to their respective differences in internal fluence resolution, an additional calculation was performed on the NovalisTX with AAA set to a resolution

Table 2: Point dose data measured with a μD for a selection of small field MLC/jaw combinations at SPD = 91.5, detph 8.5 cm (200 MU). The table lists the deviations observed for the Clinac iX and NovalisTX between measurement and calculation for different dose calculation conditions: values are shown for both algorithms at 1 mm dose calculation resolution ($AAA_{res1.0}$ and $AXB_{res1.0}$). For the Novalis, values are also listed for a 2.5 mm resolution ($AAA_{res2.5}$ and $AXB_{res2.5}$). The $AAA_{res1.25}$ calculation was added as it uses to the same internal fluence resolution as $AXB_{res2.5}$.

MLC in XxY (cm² in cm²)	Clinac iX, (120MLC)			NovalisTX (HDMLC)					
	μD (Gy)	AAA res1.0	ACUr es1.0	μD (Gy)	AAA res1.0	ACUr es1.0	AAA res2.5	ACUr es2.5	AAA res1.25
0.5x0.5 in 1x1	/	/	/	1.028	-7.56%	-10.74%	-32.74%	-69.97%	-10.74%
0.5x1 in 1x2	1.195	-2.37%	-0.58%	1.178	-5.35%	-4.57%	-12.54%	-15.98%	-7.06%
no MLC in 1x1	1.272	0.89%	0.89%	1.297	-0.20%	-0.92%	-1.95%	-3.33%	-0.71%
1x1 in 1x1	1.268	-0.61%	0.30%	1.285	-0.20%	-0.61%	-2.47%	-3.65%	-0.30%
1x1 in 2x2	1.308	-4.63%	-2.16%	1.296	-5.63%	-4.41%	-8.86%	-7.80%	-6.42%
2x2 in 3x3	1.444	0.40%	-0.10%	1.450	-2.04%	-2.88%	-3.20%	-2.77%	-0.91%
3x3 in 5x5	1.540	0.10%	-0.30%	1.535	0.89%	-0.30%	0.10%	-0.10%	0.20%
no MLC in 5x5	1.610	0.20%	0.10%	1.610	0.79%	-0.30%	0.20%	-0.3%	0.20%

of 1.25 mm, effectively obtaining the same internal fluence resolution as $AXB_{res2.5}$. As expected, results were slightly worse than for the $AAA_{res1.0}$ calculation, but still considerably better than the $AXB_{res2.5}$ results for field openings with dimensions smaller than 2cm, indicating that deviations can not be ascribed to the fluence resolution only.

The three different MLC/jaw combinations all resulting in a 1x1 cm² field opening (no MLC in a 1x1 cm² open field and 1x1 cm² MLC in 1x1 cm² and 2x2 cm² jaws) illustrate another tendency: for the smallest MLC openings, agreement between calculation and measurement improves as jaw positions approach the MLC outline. This is systematically observed for both treatment units. Although not shown in table 2, this tendency mostly manifests itself for jaw sizes smaller than 5x5 cm². For the 5x5 cm² jaw opening, all data for MLC apertures with dimensions of at least 1 cm, agree within 3% with the $AAA_{res1.0}$ and $AXB_{res1.0}$ calculation, in spite of the much larger jaw opening.

Additionally, it can be observed that the different MLC characteristics –especially the dosimetric leaf gap - between the HDMLC and the 120MLC have no noticeable impact on the absolute isocentric dose for beam aperture dimensions of 1 cm or more. Even for the 0.5x1 cm² measurements, the DLG can only be held accountable for a fraction of the 3% dose difference between measurements on the NovalisTX and on the Clinac iX as the open field output factor for the 1x2 cm² jaws already differs by 2% as well (not shown).

1D& 2D: water phantom scans and planar dose validation

In order to eliminate the absolute dose difference (MU calculation) from the depth dose evaluation, figure 8 displays the calculated depth doses for $AAA_{res1.0}$ and $AXB_{res1.0}$ at SPD 91.5 cm, normalized to the absolute dose measured in water by means of the above (table 2) established correction factor at a depth of 8.5 cm. The measured depth dose curves in figure 8 are the ones acquired with the dSRS.
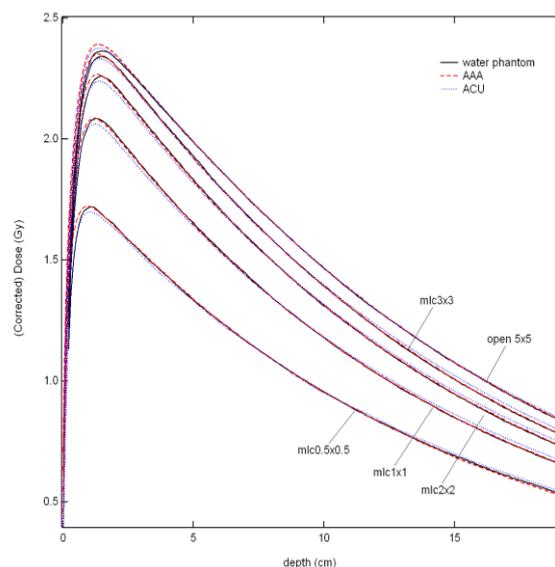
Figure 8: Comparison between measured and calculated depth dose curves for small (MLC) fields. Calculated PDDs were normalized to the measurement at 8.5 cm depth to correct for the absolute dose difference in the calculation. Except for the data in the build-up area, the relative shape of the PDD is perfectly reproduced for the $AAA_{res1.0}$ calculation while minor deviations are observed for the $AXB_{res1.0}$ data (<1%).

When ignoring the absolute difference, $AAA_{res1.0}$ produces a visually perfect reproduction of the shape of the measured small field PDD, except in the build-up area. PDDs calculated for the MLC fields with $AXB_{res1.0}$ diverge slightly (up to ~ 1%) from the measured data as the distance from the normalization point (at 8.5 cm depth) increases. The 5x5 open field depth dose, however, matches the measured one. The $AXB_{res1.0}$ dose in the build-up area also differs more from the water phantom data than the $AAA_{res1.0}$ calculated dose. Depth doses calculated at the other SPDs were similarly rescaled to the water measurement at a fixed depth (not shown) and they all demonstrate results analogous to the ones in figure 8.

The transversal profile measured (dSRS) across the MLC striped pattern is compared to both calculation algorithms in figure 4b. Overall agreement is consistent with the deviations found in the absolute point dose comparisons as a function of MLC opening: for the 0.5 cm, 1 cm and 1.5 cm wide strips, $AAA_{res1.0}$ underestimates the peak dose by 8%, 2.5% and 0.7 %, respectively, while $AXB_{res1.0}$ reports 10%, 1.3% and 0.7% too little. From the profiles, however, it can also be observed that the summit of the 0.5 cm gap is only ~ 0.1 cm wide, making the absolute dose difference very dependent on the exact location of the dose calculation grid points. Although the detector diameter (0.12 cm) is somewhat larger than the calculation grid (1 mm), the calculated profiles are slightly more diffuse than the measured profile: apart from the dose underestimation at the center of the narrow peaks, both $AAA_{res1.0}$ and $AXB_{res1.0}$ display a small broadening of the penumbra. A dose calculation with the 2.5 mm grid is only displayed for AAA in order not to overload the graph, but the results for $AXB_{res2.5}$ look equally inadequate. Following the above established inferior results for the $AAA_{res2.5}$ and $AXB_{res2.5}$ calculations, these will henceforth be excluded from the presented data.

The ~0.4 mm resolution of the portal imager permits an up-close inspection of the photon fluence as measured by the aS1000. Although the Varian portal dose prediction algorithm was not yet validated for small field dosimetry, it does provide an indirect view on the actual photon fluence used during the Eclipse dose calculation (for both AAA and AXB) as it simply convolves this fluence with a single pencil beam (and rescales it with a number of correction factors to try and obtain the expected absolute dose level). Figure 4c displays the profiles extracted from the acquired dosimetric image along with the image predictions based on the $AXB_{res1.0}$ fluence (0.5 mm resolution) and the $AAA_{res1.0}$ and $AAA_{res2.5}$ fluences (1.0 and a 2.5 mm fluence resolution, respectively). As the resolution changes from 0.5 mm to 2.5 mm, the reduction in the fluence maximum of the narrowest strip is most apparent, along with the gradual broadening of the penumbra region. For the wider strips, the maximum of the peak is not considerably affected.

3D: volumetric dose validation

Analysis of the simple, conformal arcs show near-perfect agreement (<1%) for the $AXB_{res1.0}$ calculation and a 2 to 4 % too low dose for the $AAA_{res1.0}$ calculation on the 1.5 and 1.0 cm target, respectively (figure 6a and 6b). For the 3.0 cm target, $AAA_{res1.0}$ also matches the calculation within 1 % accuracy for the conformal arc plan (not shown). For the (simple) Rapidarc plans, however, the agreement between measured and calculated 3D dose is inferior to the near-perfect results obtained for the conformal arcs. The least favorable results are now obtained for the plan made on the largest target, shown in figure 6c. Although the shape of the dose distribution appears to be adequately reproduced, the overall dose is underestimated by ~ 4 % and ~ 2% for $AAA_{res1.0}$ and $AXB_{res1.0}$, respectively. The MLC movements of these RapidArc deliveries are more modulated than those of the conformal arcs, resulting in a smaller average MLC opening compared to the jaw settings. For the RapidArc delivery shown in figure 6c, an average MLC opening of ~ 2 cm^2 moves within the 3.0x2.8 cm^2 collimator setting. The observed absolute discrepancy is therefore in accordance with what was found during the point dose validation of the different jaw/MLC combinations on the Clinac iX with the 120MLC.

3.3. Patient QA

An in-depth analysis was performed on the two test patients made for this purpose on the Clinac iX. Table 3a aims to summarize the obtained measurements compared to the dose calculations. In the left half of the table, the µD measurements in Ruby show good agreement with the dose calculations for almost all lesions. $AAA_{res1.0}$ reports a slightly lower maximum dose than $AXB_{res1.0}$, especially at the level of the smallest lesion of the '2Meta' patient. This lesion is the only one for which one of the µD measurements shows an underdosage of more than 3% for $AXB_{res1.0}$. The positive sign of the dose deviation for the Pp3D indicates that the detector's diameter is too large for this lesion. For the other lesions, however, Pp3D measurements are most satisfactory.

The right half of table 3a summarizes the evaluation by means of the 1000SRS/Oct4D systems. We judged the 3D gamma evaluation score for the 70 % isodose volume (γ_{3D} (iso70%)) to be the most representative statistical parameter for data interpretation. On Oct4D_Maxi, $AAA_{res1.0}$ calculations show inferior agreement to the measurement than $AXB_{res1.0}$ calculations. For nearly all plans, the dose tolerance needs to be relaxed to 5% to obtain a 99% PR, a condition that is already achieved for a 3% dose limit when using $AXB_{res1.0}$. This difference between AAA and AXB is only prominent in Oct4D_Maxi and not in Oct4D_Mini; illustrating that the tendency of AAA to underestimate the dose in narrow MLC openings becomes more pronounced with increasing depth. For AXB, no such depth dependence

could be deduced from the Oct4D data. Even so, nearly all plans do reach a 99% PR for the 5%L,1mm criteria. The only exception is the non-coplanar treatment of the double lesion, for which only the AXB calculation on Oct4D_Mini passed the 99% PR with a dose tolerance of at least 5%. This poor outcome is due to the inappropriate use of the total dose rather than the field-by-field evaluation. For the coplanar and nearly coplanar dose delivery, the Oct4D without couch rotation still results in a reasonable representation of the patient 3D dose distribution. For a single lesion located at isocentre, this method even holds for the radically non-coplanar arc setup ('1Meta_nonCP') as the high dose is delivered to isocentre regardless of the couch rotation. For the multiple lesions case, however, the high dose peaks are no longer situated at isocentre and the absence of the true couch rotation during QA makes the

resulting 3D dose totally unrepresentative of the patient 3D dose: high dose areas in the non-rotated phantom do not necessarily correspond to high dose areas in the patient and vice versa. As the 70% isodose becomes a clinically irrelevant parameter in this summed dose matrix, the importance of the poor outcome of the γ_{3D} (iso70%) is equally hard to judge. The different arcs of this non-coplanar dose delivery were therefore evaluated on an individual basis and each of the arcs showed a PR of the same quality as the total plans for the coplanar and nearly coplanar cases, thereby confirming the adequate agreement between dose calculation and delivery for every arc individually.

*T*able 3: Overview of the QA results obtained on SRT treatment plans verified by means of point dose measurements in Ruby and by means of the 1000SRS/Oct4D system. Parallel validations with all methods on the Clinac iX are presented in part (a): single('1M') and multiple lesions('2M') were treated with non-coplanar ('_nonCP'), coplanar ('_CP') and nearly coplanar ('_nearCP') arc geometries. For the point dose measurements in Ruby, the percent deviations between the calculated and measured dose is given for every lesion. The '2M' plans therefore have two values per plan: the smallest deviation always corresponds to the largest lesion. The right half of part (a) lists the percentages of points that pass the γ_{3D} analysis within the 70% isodose volume. Local dose difference criteria were varied fro 3%L to 5%L, while the DTA was kept fixed at 1mm. The scores are given for Oct4D_Maxi as well as for Oct4D_Mini. Part (b) of the table only lists results for Oct4D_Mini measurements compared to AAA$_{res1.0}$ dose calculations as this is what is currently used in clinical routine on the NovalisTX. Scores are shown for a representative selection of 10 patients (P1-P10).

a. Clinac iX, 120MLC

| | Ruby & μD | | Ruby & Pp3D | | Oct4D_Maxi γ_{3D} (iso70%), DTA = 1mm | | | | Oct4D_Mini γ_{3D} (iso70%), DTA = 1mm | | | |
| | | | | | AAA$_{res1.0}$ | | ACU$_{res1.0}$ | | AAA$_{res1.0}$ | | ACU$_{res1.0}$ | |
	ΔAAA$_{res1.0}$	ΔACU$_{res1.0}$	ΔAAA$_{res1.0}$	ΔACU$_{res1.0}$	3%L	5%L	3%L	5%L	3%L	5%L	3%L	5%L
1M_NonCP	-1.3%	-0.5%	-0.7%	0.1%	96.7	100	100	100	99.6	100	99.7	100
1M_CP	-2.5%	-1.2%	-1.2%	0.3%	97.8	99.8	100	100	99.6	99.8	99.7	99.9
1M_nearCP	-2.4%	-1.1%	-1.6%	-0.3%	95.1	99.1	99.6	100	99.7	100	100	100
2M_nonCP	-0.7% / -1.8%	0.1% / 0.0%	-0.8% / 4.0%	0.1% / 5.9%	84.4	92.2	94.9	97.5	92	98	94.4	99.5
2M_CP	-1.6% / -3.3%	0.0% / 0.1%	-0.6% / 5.8%	1.2% / 7.1%	98.8	100	100	100	100	100	100	100
2M_nearCP	-1.7% / -5.0%	0.1% / -3.9%	-1.5% / 6.7%	0.3% / 8.0%	98.3	100	99.7	100	99.9	100	99.8	100

b. NovalisTX, HDMLC

| | Oct4D_Mini γ_{3D} (iso70%), DTA = 1mm AAA$_{res1.0}$ | |
	3%L	5%L
P1	83.4	95.3
P2	81.6	100
P3	67.1	90.9
P4	94.4	100
P5	74.9	91.1
P6	96.9	99.9
P7	88.2	97.8

The third part of table 3 lists a representative selection of stereotactic arc treatments on the NovalisTX for which pre-treatment QA was performed with Oct4D_Mini. Results are markedly inferior to those obtained on the Clinac iX: none of the plans come even close to achieving 99% PR for the 3%L,1mm criteria and even for the lenient 5%L,1mm settings, only 4 out of 10 plans pass. As most of these are single lesion cases, the deviations can not be attributed to the use of an inappropriately summed plan for non-coplanar delivery. On the contrary, for some cases individual arcs were compared to their corresponding calculation and similarly low-grade outcomes were observed. Dose calculations with AXB$_{res1.0}$ did not bring about a systematic improvement. Only two obvious differences exist between both treatment units: the algorithm configurations and the MLC type. As it was observed during algorithm validation that for the very small MLC fields results are better for the beam data configured on the Clinac iX than those on the NovalisTX, treatment plans on the NovalisTX were recalculated with the Clinac iX algorithm version and vice versa. Although these recalculations confirmed the slight improvement when using the Clinac iX algorithm configuration, they were insufficient to explain the marked inferiority of the results for patient QA on the NovalisTX. The additional problems are therefore suspected to be related to the HDMLC, in particular to the underestimation of the dose in areas of considerable asynchronous leaf movement, resulting in a pronounced tongue and groove effect. Although the exact impact of this effect is difficult to quantify, from the leaf movement one can judge whether a dose delivery will be subject to a lot of tongue and groove effect or not. The simple observation of the leaf movement for the different plans listed in table 3 supports the hypothesis that HDMLC VMAT arcs with more pronounced asynchronous leaf movement indeed have lower pass rates.

IV. DISCUSSION

Careful and systematic benchmarking of commercially available dosimetry equipment requires time and effort but

this investment is easily won back when the practical knowledge gained from it can be put to good use when choosing an appropriate detector for a specific task at hand, when interpreting measurement results (knowing their expected precision) or when troubleshooting. Without appropriate, TPS independent benchmarking, one cannot be certain if observed deviations are detector or TPS related, or both. This is especially true for stereotactic treatments where very small dimensions and high dose (rate) delivery are combined, pushing both the detector and the dose calculation to the limits of their capabilities.

Combining the step-by-step detector evaluation with background knowledge of the dose calculation algorithm configuration firstly helps with the detector choice for beam data acquisition. When upgrading an existing AAA or AXB configuration – typically already configured down to a 3x3 cm^2 field size – to include small field dose calculation, the only data that really need to be added are the small field output factors. As all diode detectors were found to be equally suitable for this, and as most radiotherapy departments have at least one of these available, no additional purchases need to be made for this part of the stereotactic treatment implementation. Note that, while the appropriate detector choice may be important, it is also essential to carefully verify (and possibly adjust) the jaw calibration before initiating the output factor measurements.

When basic beam data for AAA and/or AXB need to be acquired from scratch, however, our preferred detector for PDD and profile scans would be the Sf3D as this detector can comfortably be used for the whole field range (from 2x2 to 40x40 cm^2). Even though depth dose and profile data for the 2x2 cm^2 field size are not actually required and contribute very little –if anything- to the algorithm configuration, the 2x2 cm^2 PDD acquisition can be put to use for the algorithm validation. The Sf3D can also be used for output factor measurements down to 3x3 cm^2, below which one needs to switch to one of the diode detectors or to the μD. Although the μD is definitely the most versatile detector as it can go down to 1x1 cm^2 (for PDDs, profiles and output factors) because of its excellent spatial resolution, on the down side it has a low sensitivity and requires considerably longer sampling times to achieve good signal-to-noise ratio. This may not look like a big disadvantage on paper, but when acquiring beam data it does start to feel like one as the evening progresses. In addition, as the 1x1 cm^2 PDD and profile scans are in any case totally ignored during the configuration process, there is little benefit in using the μD for beam data acquisition. The inferior resolution of the Sf3D is not an issue for the Eclipse basic beam data acquisition as the penumbra region is also ignored during the configuration process. However, if high resolutions profiles or small field PDDs do need to be acquired in a water phantom for purposes other than the AAA or AXB configuration, our preference would go to the dSRS because of its high sensitivity and its good agreement

with the ion chamber in the low dose areas (below the MLC or below the jaws) at all depths.

While very little – if any – additional equipment needs to be foreseen for the algorithm configuration, validation can be extremely cumbersome without the appropriate tools. Past incidences in different radiotherapy centers as well as our own validation results clearly demonstrate that accurate absolute dose calculation in small fields is not a given.

A minimum requirement for validation and subsequent patient QA would be a high resolution single detector that shows good directional independence (such as the μD or Pp3D) and a small solid water phantom in which to fit the detector (such as an assortment of small solid water blocks of several thicknesses or a phantom like Ruby). The static MLC/jaw combinations provide a simple test and a good indication of the accuracy of the absolute dose calculation that can be expected for small MLC openings in different jaw sizes. We have observed that some algorithm configurations give better results than others but we have not been able to determine the underlying cause, making it all the more advisable to effectively perform such measurements. When carried out with a single detector in a water phantom, these test do take some time, but when solid water blocks or a phantom like Ruby are available, and the plans have been prepared in Eclipse beforehand, 15 minutes machine time suffice for the whole measurement sequence. For point dose validation of the conformal and RA arc treatments during the validation process, Ruby was most successful in combination with the μD, but the Pp3D can also be used as long as one is aware of its tendency to underestimate the actual dose as field dimensions become very small ($\leq$ 1 cm). The Pp3D has the drawback of possibly reporting overly optimistic agreement for field sizes for which both the detector and the dose calculation underestimate the actual dose. Although spherical phantoms exist and have the distinct advantage of being directionally independent by design, we have a preference for geometric structures with flat surfaces as they are easy to place on the treatment couch (or couch extension), to align to the field crosshairs and lasers and they do not need any specific mounting accessory to prevent them from rolling. The geometric structure is also easily matched to its CBCT image, further facilitating accurate phantom setup. With a directionally independent detector inserted, this very simple phantom allows accurate point dose verification of the patient treatments in the exact same geometry as the actual treatment plan, including couch rotations. While the QA procedure is quite straightforward for single lesion treatments at isocentre, it becomes more cumbersome and error-prone for treatments with multiple lesions as a separate verification plan needs to be made per lesion and each time, the detector needs to be positioned at the center of the lesion rather than at isocentre. As we find that we treat more and more multiple lesions with a single isocentre, this is an important drawback. In addition, the single point dose measurement is just that: a single point dose. It does not

provide any information on the location or accuracy of the dose drop-off at the edge of the target, even though this is an important factor in stereotactic treatments. Nor can the single point measurement provide much assistance during trouble-shooting.

For a more in-depth validation, the most efficient and multipurpose validation tool by far is the 1000SRS. While high resolution profiles can indeed be acquired in a water phantom like we have done, the acquisition process is tedious and the analysis is cumbersome as it requires extensive manual data manipulation before an actual comparison with the TPS data can be performed in third party data analysis software. Great care needs to be taken when converting the measured profiles into absolute dose, but as the absolute dose level is one of the weak links in the dose calculation, this step is quite essential. As the profiles extracted from the orthogonally irradiated 1000SRS array compared so well to the water phantom profiles obtained with the µD or dSRS at all three depths (5, 10 and 15 cm), profile acquisitions in the water phantom were further abandoned and replaced by 2D planar dose measurements with the 1000SRS instead. In fact, both the small MLC output factor data (down to 0.5×0.5 cm^2) and the profile comparisons experimentally reflect a spatial resolution that would be of the order of ~1 mm instead of the 2.4 resolution defined by the actual chamber dimensions. The previously reported dose rate and field size dependences of the 1000SRS [56] were simply handled through an appropriate choice of cross-calibration conditions: we mostly used a 4x4 cm^2 or 5x5 cm^2 rather than a 10x10 cm^2 reference field and irradiated at maximum dose rate (600MU/min for 6MV, 1000MU/min for 6MV_SRS). The static validation fields were always delivered with this constant, maximum dose rate and the high dose levels of the real treatment plans cause the dose rate to always be at (or close to) its maximum level as well, even for RA treatments.

For validation of the stereotactic arc treatments, the 1000SRS needs to be combined with the Oct4D rotational phantom. Both the Oct4D_Maxi and Oct4D_Mini were validated independently of the TPS dose calculation and both were found to give equally reliable measurement based dose reconstructions. Although the 3D dose is slightly better reconstructed when phantom-specific PDD sets (PDD$_{85}$ and PDD$_{91.5}$, respectively) are used, the effect of this is only apparent in static acquisitions of single fields but hardly visible in dose reconstructions of rotational deliveries. As we now have both PDD sets available, we do alternate between them accordingly, but from a practical point of view, it can be safely assumed that a single PDD set suffices for patient QA. Although both phantom diameters produce correct dose reconstructions, there are a few practical disadvantages to the Oct4D_Maxi compared to Oct4D_Mini with respect to stereotactic plan QA. Firstly, the large diameter regularly invokes memory problems in the Eclipse TPS because of the 1 mm calculation grid (for both AAA and AXB), causing the dose calculation to fail. And even if the calculation in the full phantom is successful, the

calculation process takes a very long time and the exported dose file is so large that memory issues sometimes arise in the Verisoft software as well. It is therefore advisable to reduce the calculation volume but this needs to be done manually, hindering automated verification plan creation. In addition, our data have shown that AAA results are inferior in the large phantom. Although this is attributed to a genuine deviation in the dose calculation, it may be argued that 15 cm could be too large a depth to reflect clinical relevance, especially for intracranial stereotactic treatments. None of these issues are encountered with the Oct4D_Mini. The one drawback encountered with both Oct4D compositions, on the other hand, is the removal of planned couch rotations, in the phantom calculation as well as in the delivery. For single lesions or for multiple lesions with (nearly) coplanar treatment arcs, it is sufficient to compare the summed doses of the different arcs to the total calculated dose by means of the γ_{3D}(iso 70%) and visual assessment of the summed data. For multiple lesions treated with a single isocentre and a radically non-coplanar setup, this summed dose without couch rotation becomes totally distorted and impossible to interpret. For these cases, the results are preferably analyzed for each individual arc. Although this is more time-consuming on the analysis side, it does not add any machine time to the QA procedure and it is still much more efficient and less error-prone than the repetitive treatment delivery per lesion with Ruby.

From the algorithm validation performed on Clinac iXs and the NovalisTX, we can draw a number of general conclusions. Firstly, one conclusion holds for all dose calculations: if deviations are observed in the high dose area, they are always underestimates of the true dose. Secondly, a large error that can easily be made and subsequently overlooked is the accidental use of the 2.5 mm dose calculation grid. As the default calculation resolution is usually set to 2.5 mm for standard treatments, the planner needs to actively change this resolution when performing stereotactic treatment optimization. Fortunately, when a verification plan is created on a phantom, it uses the same calculation resolution as the plan of origin and the QA will detect the dose discrepancy. Third, near-identical looking basic beam data can result in beam configurations of different precision. This needs to be investigated further as it points towards instability in the algorithm configuration. Although it cannot be helped for now, it can at least be diagnosed, allowing the physicist to estimate beforehand how accurate the final dose calculation will be and to take this into account during plan evaluation. In our study, excellent results (<3%) were obtained on the Clinac iX units with AXB$_{res1.0}$. On the NovalisTX, this accuracy was only achieved for simple MLC field dimensions of at least 2 cm. Fourth, while the Eclipse modeling of the dynamic MLC appears satisfactory for the 120MLC, it is the cause of additional deviations for the HDMLC on the NovalisTX. The overall MLC transmission can only be modeled by a single parameter in Eclipse, regardless of the leaf width.

While a sensible average value for all leaves can be determined for the 120MLC, for the HDMLC the overall MLC transmission is noticeably higher for the high definition central leaves than for the outer leaves. Even more important than the transmission could be the tongue and groove model. The dose calculation is too low in areas irradiated through highly asynchronous leaf movement. This effect is moderate for the 120MLC but can go up to 8% for the HDMLC. As a result of the above, ironically, dosimetric results for the stereotactic treatments are better on the conventional Clinac iX units than on the NovalisTX.

Having benchmarked the QA equipment and the dose calculation precision, a decision needs to be made regarding the acceptance criteria to be used for patient QA. The traditional 3%G,3mm gamma evaluation (with a 95 % pass rate) is ill adapted to the clinical needs of stereotactic treatments on almost all aspects. Firstly, it would be unrealistic to state that a 3% accuracy in the high dose area is mandatory. Given the traditional dose prescription to the 50, 70 or 80% isodose level (depending on the delivery approach) around the target and the ensuing dose non-uniformity within the target, dose homogeneity in the target is not the goal in stereotactic treatment planning. The goal is to achieve the prescribed lower dose limit tightly shaped around the target. Within the target, the dose can go up to 100%, but there is no consensus on whether or not this is clinically necessary. Underestimating the true dose to the lesion by a few percent is therefore no cause for alarm. However, when deviations become larger than e.g. 5%, the clinician's opinion could be invoked to decide whether the measured overdosage at the level of the lesion is acceptable. Secondly, while we are willing to be considerably more lenient on the maximum dose at the level of the lesion, we do not wish to allow for a 3 mm imprecision on the penumbra. The spatial precision of the gradient fall-off is an important aspect of the treatment. The DTA is therefore set to 1 mm. Admittedly, this is very close to the positional precision that can be achieved with the 1000SRS/Oct4D phantom setup. It is therefore sometimes necessary to perform an alignment of the measured and calculated 3D dose matrices in the Verisoft software. From the validation of a cohort of real patient plans, we have found that a 5%L,1mm gamma analysis on the 70% isodose volume gives a score that is representative for the clinically relevant agreement between measurement and calculation. Even so, we use this gamma analysis only as a guideline rather than as a pass/fail filter. We find that for these small volumes, for now, visual inspection of the data in e.g. the three orthogonal planes provides the most relevant and efficient analysis.

V. CONCLUSION

A compact procedure for benchmarking the different detector systems (from point dose to 3D dose) eligible for SRT measurements provided a clear and practical overview regarding their expected accuracy and their possible applications:

Embedding small field dose calculations into an already existing AAA and AXB algorithm configuration merely requires the additional input of small field output factors (down to 1x1 cm^2). For this, all diodes and the μD were found to be suitable. As quality and safety guidelines on SRT stress the need for TPS validation as well as patient-specific treatment QA, it is advantageous to select multipurpose detector systems that can serve for both. A single detector that is directionally independent is mandatory to permit verification of the total dose delivered through non-coplanar arcs. The μD is most suitable for this, but the Pp3D can also be used. When inserted into a phantom such as Ruby, the single detector can be used for the most basic validation of the TPS as well as for the most complex RA dose verification. The point dose measurement provides a relevant verification of the dosimetric precision of the high dose level (in static or arc delivery), but does not provide any reassurance on the location of the dose fall-off. The latter can easily and reliably be verified with the 1000SRS/Oct4D combination. Whereas the Oct4D_Mini has some practical advantages over the Oct4D_Maxi, both systems were carefully validated and – when appropriately cross-calibrated - provide equally reliable measurement-based dose reconstructions.

Using the above selected detector systems, AAA and AXB validation on the Clinac iX (120MLC) and the NovalisTX (HDMLC) revealed differences in algorithm precision between different treatment units. As the origin of this difference remains unknown, it further emphasizes the need to validate individual algorithm configurations. It was also found that the Eclipse modeling of the HDMLC should be further improved, especially with respect to the tongue and groove effect. On the Clinac iX, the obtained results were excellent for AXB and AAA, undoubtedly within clinical acceptance. On the NovalisTX, results were inferior to the Clinac iX. Because of the above mentioned deviations, the calculated dose systematically underestimated the real dose by a few percent (2-7%, depending on the patient plan). But also for the NovalisTX, all results were judged to be within clinical acceptance for SRT treatments.

wishes to express appreciation to the Varian Helsinki team for their assistance and feedback.

The authors have no relevant conflicts of interest to disclose.

REFERENCES

[1] R. Timmerman, R. Paulus, J. Galvin, J. Michalski, W. Staube, J. Bradley, A. Fakiris, A. Bezjak, G. Videtic, D. Johnstone,J. Fowler,E. Gore, and H. Choy. "Stereotactic body radiation therapy for inoperable early stage lung cancer," JAMA 303, 1070-1076 (2010). doi: 10.1001/jama.2010.261

[2] D.E. Heron, R.L. Ferris, M. Karamouzis M, R.S. Andrade, E.L. Deeb, S. Burton, W.E. Gooding, B.F. Branstetter, J.M. Mountz, J.T. Johnson, A. Argiris, J.R. Grandis, and S.Y. Lai. "Stereotactic body radiotherapy for recurrent squamous cell carcinoma of the head and neck: results of a phase I dose-escalation trial," Int. J. Radiat. Oncol., Biol., Phys., 75(5), 1493-1500 (2009). doi: 10.1016/j.ijrobp.2008.12.075

[3] P. Baumann, J. Nyman, M. Hoyer, B. Wennberg, G. Gagliardi, I. Lax, N. Drugge, L. Ekberg, S. Friesland, K.A. Johansson, J.A. Lund, E. Morhed, K. Nilsson, N. Levin, M. Paludan, C. Sederholm, A. Traberg, L. Wittgren, and R. Lewensohn. "Outcome in a prospective phase II trial of medically inoperable stage I non-small-cell lung cancer patients treated with stereotactic body radiotherapy," J. Clin Oncol. 27, 3290-3296 (2009). doi: 10.1200/JCO.2008.21.5681

[4] K.E. Rusthoven, B.D. Kavanagh, H. Cardenes, V.W. Stieber, S.H. Burri, S.J. Feigenberg, M.A. Chidel, T.J. Pugh, W. Franklin, M. Kane, L.E. Gaspar, and T.E. Schefter. "Multi-institutional phase I/II trial of stereotactic body radiation therapy for liver metastases," J. Clin. Oncol. 27,1572-1578 (2009). doi: 10.1200/JCO.2008.19.6329

[5] K.E. Rusthoven KE, B.D. Kavanagh, S.H. Burri, C. Chen, H. Cardenes, M.A. Chidel, T.J. Pugh, M. Kane, L.E. Gaspar, and T.E. Schefter. "Multi-institutional phase I/II trial of stereotactic body radiation therapy for lung metastases," J Clin Oncol. 27, 1579-1584. (2009). doi: 10.1200/JCO.2008.19.6386

[6] M.T. Lee, J.J. Kim, R. Dinniwell, J. Brierley, G. Lockwood, R. Wong, B. Cummings, J. Ringash, R.V. Tse, J.J. Knox, and L.A. Dawson. "Phase I study of individualized stereotactic body radiotherapy of liver metastases," J. Clin Oncol. 27, 1585-1591 (2009). doi: 10.1200/JCO.2008.20.0600

[7] A.J. Fakiris, R.C. McGarry, C.T. Yiannoutsos, L. Papiez, M. Williams, M.A. Henderson, and R. Timmerman. "Stereotactic body radiation therapy for early-stage non-small-cell lung carcinoma: four-year results of a prospective phase II study," Int. J. Radiat. Oncol., Biol., Phys. 75, 677-682 (2009). doi: 10.1016/j.ijrobp.2008.11.042

[8] P. Baumann, J. Nyman, M. Hoyer, G. Gagliardi, I. Lax, B. Wennberg, N. Drugge, L. Ekberg, S. Friesland, K.A. Johansson, J.S. Lund, E. Morhed, K. Nilsson, N. Levin, M. Paludan, C. Sederholm, A. Traberg, L. Wittgren, and R. Lewensohn. "Stereotactic body radiotherapy for medically inoperable patients with stage I non-small cell lung cancer - a first report of toxicity related to COPD/CVD in a non-randomized prospective phase II study," Radiother. Oncol. 88, 359-367 (2008). doi: 10.1016/j.radonc.2008.07.019

[9] C.R. King, J.D. Brooks, H. Gill, T. Pawlicki, C. Cotrutz, and J.C. Presti "Stereotactic body radiotherapy for localized prostate cancer: interim results of a prospective phase II clinical trial," Int. J. Radiat. Oncol., Biol., Phys. 73,1043-1048 (2009). doi: 10.1016/j.ijrobp.2008.05.059

[10] R.V. Tse, M. Hawkins, G. Lockwood, J.J. Kim, B. Cummings, J. Knox, M. Sherman, and L.A. Dawson. "Phase I study of individualized stereotactic body radiotherapy for hepatocellular carcinoma and intrahepatic cholangiocarcinoma," J. Clin. Oncol. 26, 657-664 (2008). doi: 10.1200/JCO.2007.14.3529

[11] E.L. Chang, A.S. Shiu, E. Mendel, L.A. Mathews, A. Mahajan, P.K. Allen, J.S. Weinberg, B.W. Brown, X.S. Wang, S.Y. Woo, C. Cleeland, M.H. Maor, and L.D. Rhines. "Phase I/II study of stereotactic body radiotherapy for spinal metastasis and its pattern of failure," J. Neurosurg. Spine. 7,151-60 (2007). doi: 10.3171/SPI-07/08/151

[12] M.T. Milano, A.W. Katz, A.G. Muhs, A. Philip, D.J. Buchholz, M.C. Schell, and P. Okunieff. "A prospective pilot study of curative-intent stereotactic body radiation therapy in patients with 5 or fewer oligometastatic lesions," Cancer. 112, 650-658 (2008). doi: 10.1002/cncr.23209

[13] S.E. Combs, T. Welzel, D. Schulz-Ertner, P.E. Huber, and J. Debus. "Differences in clinical results after linac-based single-dose radiosurgery versus fractionated stereotactic radiotherapy for patients with vestibular schwannomas," Int. J. Radiat. Oncol., Biol., Phys. 76, 193-200 (2010). doi: 10.1016/j.ijrobp.2009.01.064

[14] T.D. Solberg, J.M. Balter, S.H. Benedict, B. A. Fraass, B. Kavanagh, C. Miyamoto, T. Pawlicki, L. Potters, and Y. Yamada, "Quality and Safety Considerations in Stereotactic Radiosurgery and Stereotactic Body Radiation Therapy," Practical Radiation Oncology, supplement material 2, 2-9 (2012) doi:10.1016/j.prro.2011.06.014

[15] P.Y. Borius, B. Debono, I. Latorzeff, J.A. Lotterie, J.Y. Plas, E. Cassol, P. Bousquet, F. Loubes, P. Duthil, A. Durand, F. Caire, A. Redon, I. Berry, J. Sabatier, and Y. Lazorthes. "Dosimetric stereotactic radiosurgical accident: Study of 33 patients treated for brain metastases," Neurochirurgie. 56:368-373 (2010). doi: 10.1016/j.neuchi.2010.07.002

[16]. S. Derreumaux, C. Etard, C. Huet, F. Trompier, I. Clairand, J.F. Bottollier-Depois, B. Aubert, and P. Gourmelon. "Lessons from recent accidents in radiation therapy in France," Rad. Prot. Dosim. 131,130-135 (2010). doi: 10.1093/rpd/ncn235

[17] P. Gourmelon, E. Bey, T. De Revel, and J.J. Lataillade. "The French radiation accident experience: emerging concepts in radiation burn and ARS therapies and

in brain radiopathology," Radioprotection. 43(5), 23-26 (2008). doi: 10.1051/radiopro:2008761

[18] W. Bogdanich, K. Rebelo, "The Radiation Boom - A Pinpoint Beam Strays Invisibly, Harming Instead of Healing," The New York Times, New York, A1 (2010).

[19]. Elekta Bulletin 98-02-17, Leksell Gamma Knife, ''New 4-mm Helmet Output Factor,'' Feb. 17, (1998).

[20]. J.P. Gibbons, D. Mihailidis, C. Worthington, H. Alkhatib, R. Boulware, R. Clark, B. Dial, and W. Neglia. "The effect of the 4-mm-collimator output factor on gamma knife dose distributions," J. Appl. Clin. Med. Phys. 4,386-389 (2003). doi: 10.1120/1.1621375

[21] H. D. Kubo, C. T. Pappas, and R. B. Wilder, "A comparison of arc-based and static mini-multileaf collimator-based radiosurgery treatment plans," Radiother. Oncol. 45, 89-93 (1997).

[22] D. Leavitt, "Beam shaping for SRT/SRS," Med. Dosim. 23, 229-236 (1998).

[23] D. Solberg, K.L. Boedeker, R. Fogg, M.T. Selch, and A.A. DeSalles, "Dynamic arc radiosurgery field shaping: A comparison with static field conformal and noncoplanar circular arcs," Int. J. Radiat. Oncol., Biol., Phys. 49, 1481-1491 (2001).

[24] H. Benedict, F.J. Bova, B. Clark, S.J. Goetsch, W.H. Hinson, D.D. Leavitt, D.J. Schlesinger, and K.M. Yenice, "Anniversary Paper: The role of medical physicists in developing stereotactic radiosurgery," Med. Phys. 35, 4262-4277 (2008). doi: 10.1118/1.2969268

[25] J. Hazard, B. Wang, T.B. Skidmore, S.S. Chern, B.J. Salter, R.L. Jensen, and D.C. Shrieve, "Conformity of LINAC-based stereotactic radiosurgery using dynamic conformal arcs and micro-multileaf collimator," Int. J. Radiat. Oncol., Biol., Phys. 73, 562-570 (2009). doi: 10.1016/j.ijrobp.2008.04.026

[26] Y. Tsuruta, M.u Nakata, M. Nakamura, Y. Matsuo, K. Higashimura, H. Monzen, T. Mizowaki, and M. Hiraoka, "Dosimetric comparison of Acuros XB, AAA, and XVMC in stereotactic body radiotherapy for lung cancer," Med. Phys. 41(8) , 081715 (2014)
doi: 10.1118/1.4890592

[27] A. Fogliata, A. Clivio, G. Nicolini, E. Vanetti, and L. Cozzi, "Intensity modulation with photons for benign intracranial tumours: A planning comparison of volumetric single arc, helical arc and fixed gantry techniques," Radiother. Oncol. 89, 254–262 (2009). doi: 10.1016/j.radonc.2008.07.021

[28] F. Lagerwaard, O. Meijer, E. van der Hoorn, W. Verbakel, B. Slotman, and S. Senan, "Volumetric modulated arc radiotherapy for vestibular schwannomas," Int. J. Radiat. Oncol., Biol., Phys. 74, 610–615 (2009). doi: 10.1016/j.ijrobp.2008.12.076

[29] S. Subramanian, C. Srinivas, K. Ramalingam, M. Babaiah, S. T. Swamy, G. Arun, M. Kathirvel, S. Ashok, A. Clivio, A. Fogliata, G. Nicolini, K. S. Rao, T. P. Reddy, J. Amit, E. Vanetti, and L. Cozzi, "Volumetric Modulated Arc-based hypofractionated stereotactic radiotherapy for the treatment of selective intracranial arteriovenous

malformations: Dosimetric report and early clinical experience," Int. J. Radiat. Oncol., Biol. Phys. 82(3), 1278-1284 (2012). doi: 10.1016/j.ijrobp.2011.02.005

[30] W. Verbakel, S. Senan, J. Cuijpers, B. Slotman, and F. Lagerwaard, "Rapid delivery of stereotactic radiotherapy for peripheral lung tumors using volumetric intensity modulated arcs," Radiother. Oncol. 93, 122–124 (2009). doi: 10.1016/j.ijrobp.2009.03.029

[31] C. Ong, D. Palma, W. Verbakel, B. Slotman, and S. Senan, "Treatment of large stage I-II lung tumors using stereotactic body radiotherapy (SBRT): Planning considerations and early toxicity," Radiother. Oncol. 97, 431–436 (2010). doi: 10.1016/j.radonc.2010.10.003

[32] C. Ong, W. Verbakel, J. Cuijpers, B. Slotman, F. Lagerwaard, and S. Senan, "Stereotactic radiotherapy for peripheral lung tumors: A comparison of volumetric modulated arc therapy with 3 other delivery techniques," Radiother. Oncol. 97, 437–442 (2010). doi: 10.1016/j.radonc.2010.09.027

[33] C. Ong, W. Verbakel, J. Cuijpers, B. Slotman, and S. Senan, "Dosimetric impact of interplay effect on rapidarc lung stereotactic treatment delivery," Int. J. Radiat. Oncol., Biol., Phys. 79, 305–311 (2011). doi: 10.1016/j.ijrobp.2010.02.059

[34] D. Palma, J. van Sömsen de Koste, W. Verbakel, A. Vincent, and S. Senan, "Lung density changes after stereotactic radiotherapy: A quantitative analysis in 50 patients," Int. J. Radiat. Oncol., Biol., Phys. 81(4),974-978 (2011). doi: 10.1016/j.ijrobp.2010.07.025

[35] D. Palma, S. Senan, C. Haasbeek, W. Verbakel, A. Vincent, and F. Lagerwaard, "Radiological and clinical pneumonitis after stereotactic lung radiotherapy: A matched analysis of three dimensional conformal and volumetric modulated arc therapy techniques," Int. J. Radiat. Oncol., Biol.,Phys. 80, 506–513 (2011). doi: 10.1016/j.ijrobp.2010.02.032

[36] M. Bignardi, L. Cozzi, A. Fogliata, P. Lattuada, P. Mancosu, P. Navarria, G. Urso, S. Vigorito, and M. Scorsetti, "Critical appraisal of volumetric modulated arc therapy in stereotactic body radiation therapy for metastases to abdominal lymph nodes," Int. J. Radiat. Oncol., Biol., Phys. 75, 1570–1577 (2009). doi: 10.1016/j.ijrobp.2009.05.035

[37] M. Scorsetti, M. Bignardi, F. Alongi, A. Fogliata, P. Mancosu, P. Navarria, S. Castiglioni, S. Pentimalli, A. Tozzi, and L. Cozzi, "Stereotactic body radiation therapy for abdominal targets using volumetric intensity modulated arc therapy with RapidArc: feasibility and clinical preliminary results," Acta Oncol. 50, 528–538 (2011). doi: 10.3109/0284186X.2011.558522

[38] L. S. Fog, J. F. B. Rasmussen, M. Aznar, F. Kjær-Kristoffersen, I. R. Vogelius, S. A. Engelhom, and J. P. Bangsgaard, "A closer look at RapidArc radiosurgery plans using very small fields," Phys. Med. Biol. 56, 1853–1863 (2011). doi: 10.1088/0031-9155/56/6/020

[39] G. Clark, R. Popple, P.E. Young, and J. Fiveash, "Feasibility of single iso-centre volumetric modulated arc

radiosurgery for treatment of multiple brain metastases," Int.J.Radiat.Oncol.,Biol., Phys. 76, 296-302 (2010). doi: 10.1016/j.ijrobp.2009.05.029

[40] C. Mayo, L. Ding, A. Addesa, S. Kadish, T. Fitzgerald, and R. Moser, "Initial experience with volumetric IMRT (RapidArc) for intracranial stereotactic radiosurgery," Int. J. Radiat.Oncol.,Biol., Phys. 78, 1457-1466 (2010). doi: 10.1016/j.ijrobp.2009.10.005

[41] H. Wolff, D. Wagner, H. Christiansen, C. Hess, and H. Vorwerk, "Single fraction radiosurgery using RapidArc for treatment of intracranial targets," Radiat. Oncol. 5 (2010). doi: 10.1186/1748-717X-5-77

[42] A. Fogliata, G. Nicolini, A. Clivio, E. Vanetti, and L. Cozzi, "Accuracy of Acuros XB and AAA dose calculation for small fields with reference to RapidArc® stereotactic treatments," Med. Phys. 38, 6228-6237 (2011). doi: 10.1118/1.3654739

[43] R. Alfonso, P. Andreo, R. Capote, M. Saiful Huq, W. Kilby, P. Kjäll, T. R. Mackie, H. Palmans, K. Rosser, J. Seuntjens, W. Ullrich, S. Vatnitsky "A new formalism for reference dosimetry of small and non-standard fields," Med. Phys. 35, 5179–86 (2008) doi: 10.1118/1.3005481

[44] IPEM, Small Field MV Photon Dosimetry, IPEM Report No. 103 (Institute of Physics and Engineering in Medicine, New York, (2010).

[45] M. Schwedas, M. Scheithauer, T. Wiezorek, T.G. Wendt, "Radiophysical characteristics of different detectors for use in dosimetry." Z. Med. Phys. 17, 172-179 (2007).

[46] M. Bucciolini, F. B. Buonamici, S. Mazzocchi, C. De Angelis, S. Onori, and G. A. Cirrone, "Diamond detector versus silicon diode and ion chamber in photon beams of different energy and field size," Med. Phys. 30, 2149–2154 (2003). doi: 10.1118/1.1591431

[47] A. Ralston, M. Tyler,P. Liu,D. McKenzie and N. Suchowerska, " Over-response of synthetic microdiamond detectors in small radiation fields." Phys. Med. Biol. 59, 5873–81 (2014) doi: 10.1088/0031-9155/59/19/5873

[48] T. Underwood, B. Rowland, R. Ferrand and L. Vieillevigne, "Application of the Exradin W1 scintillator to determine Ediode 60017 and microdiamond 60019 correction factors for relative dosimetry within small MV and FFF fields." Phys. Med. Biol. 60, 6669–83 (2015) doi: 10.1088/0031-9155/60/17/6669

[49] P. Francescon, W. Kilby, J.M. Noll, L. Masi, N. Satariano and S. Russo, "Monte Carlo simulated corrections for beam commissioning measurements with circular and MLC shaped fields on the CyberKnife M6 System: a study including diode, microchamber, point scintillator, and synthetic microdiamond detectors." Phys. Med. Biol. 62, 1076–1095 (2017) doi: 10.1088/1361-6560/aa5610

[50] A. Ralston, P. Liu, K. Warrener, D. McKenzie and N. Suchowerska, "Small field diode correction factors derived using an air core fibre optic scintillation dosimeter and EBT2 film," Phys. Med. Biol. 57, 9 (2012) doi: 10.1088/0031-9155/57/9/2587

[51] J.E. Morales, S.B. Crowe, R. Hill, N. Freeman and J.V. Trapp, "Dosimetry of cone-defined stereotactic radiosurgery fields with a commercial synthetic diamond detector." Med. Phys. 41 111702 (2014) doi: 10.1118/1.4895827

[52] A. Chalkley and G. Heyes, "Evaluation of a synthetic single-crystal diamond detector for relative dosimetry measurements on a CyberKnife" Br. J. Radiol. 87 20130768 (2014) doi: 10.1259/bjr.20130768

[53] W. Lutz, K.R. Winston,and N. Maleki. "A system for stereotactic radiosurgery with a linear accelerator," Int J Radiat Oncol Biol Phys. 14(2), 373-381 (1998).

[54] A. Van Esch, D.P. Huyskens, C.F. Behrens, E. Samsoe, M. Sjolin, U. Bjelkengren, D. Sjostrom, C. Clermont, L. Hambach, and F. Sergent, "Implementing RapidArc into clinical routine: a comprehensive program from machine QA to TPS validation and patient QA," Med Phys. 38(9),5146-66 (2011). doi: 10.1118/1.3622672.

[55] A. Van Esch, K. Basta, M. Evrard, M. Ghislain, F. Sergent, and D. P. Huyskens, "The Octavius1500 2D ion chamber array and its associated phantoms: Dosimetric characterization of a new prototype" Med. Phys. 41, 091708 (2014) doi: 10.1118/1.4892178

[56] B. Poppe, T. S. Stelljes, H. K. Looe, N. Chofor, D. Harder and K. Willborn, "Performance parameters of a liquid filled ionization chamber array," Med. Phys.40, 082106 (2013). doi 10.1118/1.4816298

[57] A. Van Esch, D.P. Huyskens, L. Hirschi, C. Baltes, "Optimized Varian aSi portal dosimetry: development of datasets for collective use," J Appl Clin Med Phys. 14(6), 4286 (2013).doi: 10.1120/jacmp.v14i6.4286.

[58] E. Sham, J. Seuntjens, S. Devic, and E. B. Podgorsak, "Influence of focal spot on characteristics of very small diameter radiosurgical beams," Med. Phys. 35, 3317–3330 (2008). doi: 10.1118/1.2936335

[59] A. Van Esch, J. Bohsung, P. Sorvari, M. Tenhunen, M. Paiusco, M. Iori, P. Engström, H. Nyström, and D. P. Huyskens, "Acceptance tests and quality control_QC_ procedures for the clinical implementation of IMRT using inverse planning and the sliding window technique: experience from five radiotherapy departments," Radiother. Oncol. 65, 53-70 (2002)

author to whom correspondence should be addressed:
ann.vanesch@7sigma.be